Geophysical Journal International

Geophys. J. Int. (2010) **183,** 390–406 doi: 10.1111/j.1365-246X.2010.04748.x

Asperities and barriers on the seismogenic zone in North Chile: state-of-the-art after the 2007 *M*w 7.7 Tocopilla earthquake inferred by GPS and InSAR data

M. Béjar-Pizarro,[1,2] D. Carrizo,[1,3] A. Socquet,[1] R. Armijo,[1] S. Barrientos,[3*] F. Bondoux,[4*] S. Bonvalot,[4*] J. Campos,[3*] D. Comte,[3*] J. B. de Chabalier,[1*] O. Charade,[5*] A. Delorme,[1*] G. Gabalda,[4*] J. Galetzka,[6*] J. Genrich,[6*] A. Nercessian,[1*] M. Olcay,[7*] F. Ortega,[6*] I. Ortega,[3*] D. Remy,[4*] J. C. Ruegg,[1*] M. Simons,[6*] C. Valderas[3*] and C. Vigny[8*]

[1]*Institut de Physique du Globe,* 4 *Place Jussieu,* 75251 *Paris Cedex* 05*, France. E-mail: bejarpi@ipgp.jussieu.fr*
[2]*Departamento de Geodinámica, Facultad de Ciencias Geológicas, Univ. Complutense,* 28040 *Madrid, Spain*
[3]*Departamento de Geofísica, Universidad de Chile, Casilla* 2777*, Santiago, Chile*
[4]*Institut de Recherche pour le Développement (IRD), UMR* 5563*/LMTG (Université de Toulouse, CNRS, IRD, OMP),* 31450 *Toulouse, France*
[5]*Division Technique de l'INSU, Meudon, France*
[6]*Seismological Laboratory, Division of Geological and Planetary Sciences, California Institute of Technology,* 1200 *E. California Blvd* 252-21*, Pasadena, CA* 91125*, USA*
[7]*Universidad Arturo Pratt, Iquique, Chile*
[8]*Laboratoire de Géologie, Ecole Normale Supérieure (ENS), CNRS,* 75231 *Paris, France*

Accepted 2010 July 20. Received 2010 July 19; in original form 2009 December 18

SUMMARY

The *M*w 7.7 2007 November 14 earthquake had an epicentre located close to the city of Tocopilla, at the southern end of a known seismic gap in North Chile. Through modelling of Global Positioning System (GPS) and radar interferometry (InSAR) data, we show that this event ruptured the deeper part of the seismogenic interface (30–50 km) and did not reach the surface. The earthquake initiated at the hypocentre and was arrested ∼150 km south, beneath the Mejillones Peninsula, an area already identified as an important structural barrier between two segments of the Peru–Chile subduction zone. Our preferred models for the Tocopilla main shock show slip concentrated in two main asperities, consistent with previous inversions of seismological data. Slip appears to have propagated towards relatively shallow depths at its southern extremity, under the Mejillones Peninsula. Our analysis of post-seismic deformation suggests that small but still significant post-seismic slip occurred within the first 10 d after the main shock, and that it was mostly concentrated at the southern end of the rupture. The post-seismic deformation occurring in this period represents ∼12–19 per cent of the coseismic deformation, of which ∼30–55 per cent has been released aseismically. Post-seismic slip appears to concentrate within regions that exhibit low coseismic slip, suggesting that the afterslip distribution during the first month of the post-seismic interval complements the coseismic slip. The 2007 Tocopilla earthquake released only ∼2.5 per cent of the moment deficit accumulated on the interface during the past 130 yr and may be regarded as a possible precursor of a larger subduction earthquake rupturing partially or completely the 500-km-long North Chile seismic gap.

Key words: Satellite geodesy; Earthquake ground motions; Subduction zone processes; South America.

1 INTRODUCTION

Our aim is a better understanding of earthquake rupture ends, specifically the regions where ruptures generated by great subduction earthquakes terminate, downdip, updip and laterally along strike. The region of the subduction interface where earthquake ruptures terminate at depth is interpreted as a transitional zone characterized by alternating transient aseismic shear and seismic slip (Hyndman & Wang 1993). The interaction between deformation processes occurring in this region and in the shallower subduction interface

*North Chile geodetic team.

seems important during the nucleation (and propagation or inhibition) of the seismic rupture. For example, it has been suggested that slow slip events occurring in the deeper region of the seismogenic zone may have triggered large earthquakes in the updip region (such as the giant 1960 Chile earthquake, Cifuentes & Silver 1989 and the *M* 8.1 1944 Tonankai earthquake in Japan, Mogi 1985). Transient aseismic slip is also observed as post-seismic afterslip in both the lower region and the upper region of the seismogenic zone, thus apparently in areas surrounding the main asperity characterized by high coseismic slip (e.g. Chlieh *et al.* 2004; Miyazaki *et al.* 2004; Baba *et al.* 2006; Hsu *et al.* 2006; Pritchard & Simons 2006). So frictional properties along the subduction interface appear distributed heterogeneously (e.g. Bilek & Lay 2002; Song & Simons 2003; Schwartz & Rokosky 2007). The best examples of frictional heterogeneities are found near lateral barriers arresting rupture propagation of large subduction earthquakes. Those barriers are often associated with structural complexities or discontinuities of the subduction interface and expressed over the long term at the Earth's surface as geomorphic features, such as peninsulas (e.g. Kii Peninsula in Japan, Ilo Peninsula in Peru and Arauco and Mejillones Peninsulas in Chile).

Here we address in some detail the problem of coseismic and post-seismic slip distribution at earthquake rupture ends by studying the surface deformation associated with the 2007 November 14 *M*w 7.7 Tocopilla subduction earthquake and its relation with the ongoing seismic cycle of large earthquakes in northern Chile. The 2007 earthquake is the last large event that has occurred in that region, which has been identified as a gap awaiting for the occurrence of a very large earthquake (Kelleher 1972; Nishenko 1985) and where it has been observed a conspicuous interplay of large earthquake ruptures around the Mejillones Peninsula, a feature identified as an important structural barrier (Armijo & Thiele 1990; Ruegg *et al.* 1996).

We use space geodesy data [InSAR and Global Positioning System (GPS)] covering the coseismic period and 1 month of post-seismic deformation. The extremely arid climate of the region is appropriate for using InSAR technique (Chlieh *et al.* 2004). We combine the InSAR results with GPS measurements acquired by the permanent network that covers the seismic gap (operated by Institut de Physique du Globe de Paris, Caltech, Departamento de Geofisica Universidad de Chile and Institut de Recherche pour le Développement). We explore the geometric parameters of the rupture by assuming uniform slip on the fault. Then we estimate the slip distribution corresponding to the main shock, to the largest aftershock and to the post-seismic deformation observed during the first month following the main event. Our results allow us to determine the evolution of coseismic and post-seismic slip distribution in space and time. We discuss the main features of the Tocopilla earthquake rupture with regard to possible slow and/or aseismic slip occurring in the deeper region, as well as to complete rupture during a very large earthquake (larger than 2007), including the updip region of the seismogenic zone. We also discuss the possible role of the Mejillones Peninsula barrier.

2 TECTONIC CONTEXT, PREVIOUS SEISMICITY AND DEFORMATION

In North Chile, the fast convergence of the Nazca and South American plates (∼65–70 mm yr^{-1}, Angermann *et al.* 1999; Bevis *et al.* 1999; Norabuena *et al.* 1999; Sella *et al.* 2002; Vigny *et al.* 2009) appears mostly accommodated by large interplate earthquakes (Comte & Pardo 1991). The lower boundary of the seismically coupled interface is located at 40–50 km, as deduced from background seismicity (Tichelaar & Ruff 1991; Comte & Suárez 1995; Delouis *et al.* 1996) and from geodetic measurements of interseismic strain (50 km depth after Bevis *et al.* 2001; 55 km depth after Khazaradze & Klotz 2003; 35 km depth and a partially coupled zone between 35–55 km after Chlieh *et al.* 2004). The region between the Ilo Peninsula (15.5°S, South Peru) and the Mejillones Peninsula (23.5°S, North Chile) represents the remaining unbroken part of a previously identified major seismic gap not having experienced a significant subduction earthquake since the South Peru (*M*w = 8.8, 1868 August 16) and the Iquique (*M*w = 8.8, 1877 May 10) megathrust earthquakes (Dorbath *et al.* 1990; Comte & Pardo 1991, Fig. 1). The 1995 *M*w 8.1 Antofagasta and the 2001 *M*w 8.4 Arequipa earthquakes appear to have provided an extra load at both extremities of the remaining ∼500 km length unruptured segment. After the 1877 event and before the 2007 Tocopilla earthquake, a few *M*s ∼seven events have been reported in the region (Comte & Pardo 1991; Tichelaar & Ruff 1991; Engdahl & Villaseñor 2002, Fig. 1) but they were not large enough to release a significant part of the ∼9 m of slip deficit accumulated in the gap in the last 130 yr. Therefore a possible future megathrust earthquake might break the remaining seismic gap. That was the situation when the *M*w 7.7 Tocopilla earthquake occurred on 2007 November 14. The first studies of this earthquake suggest that the rupture locates in the deeper part of the seismogenic interface (Delouis *et al.* 2009; Peyrat *et al.* 2010; Loveless *et al.* 2009) and that it did not rupture the whole length of the gap. Rupture initiated in the subduction interface beneath the region of the city of Tocopilla and stopped to the south when it reached the region of the subduction interface beneath the Mejillones Peninsula (Delouis *et al.* 2009; Peyrat *et al.* 2010). Most of the aftershocks following the 2007 event were concentrated immediately to the north of that peninsula (Fig. 2), a large geomorphic feature that seems to act both as a barrier arresting rupture of large earthquakes (e.g. *M* 8.8 1877 Iquique earthquake, Comte & Pardo 1991) and as an asperity where large earthquakes nucleate (e.g. *M*w 8.1 1995 Antofagasta earthquake, Ruegg *et al.* 1996). From a tectonic point of view the Mejillones Peninsula is an uplifted block under E–W extension, affected by large normal faults (Armijo & Thiele 1990; Allmendinger & Gonzalez 2009), located at the southern limit of the subduction of the Iquique Ridge (e.g. Rosenbaum *et al.* 2005). The subduction zone below this peninsula seems to concentrate aseismic afterslip (Chlieh *et al.* 2004; Pritchard & Simons 2006).

Both seismic and aseismic slip has been reported to occur in the deeper region of the seismogenic interface of North Chile. In 1997 (2 yr after the Antofagasta earthquake), an aseismic slip pulse appears to have occurred downdip the 1995 Antofagasta rupture and it may have triggered the *M*w 7.1 earthquake that occurred 1 yr later in the region immediately downdip of the aseismic pulse (Pritchard & Simons 2006). In addition to this *M*w 7.1 earthquake, other seismic events comparable both in magnitude and depth with the 2007 *M*w 7.7 Tocopilla earthquake occurred earlier in the segments north and south of the Mejillones Peninsula. In 1987, a *M*w 7.5 earthquake ruptured the region of the subduction interface immediately downdip of the subsequent 1995 rupture and was thought to have a causal relationship with this event (Ihmlé & Ruegg 1997). North of the Mejillones Peninsula, a *M*w 7.4 earthquake occurred on 1967 December 21 at a depth of 45–48 km (Malgrange & Madariaga 1983; Tichelaar & Ruff 1991) immediately north of the 2007 rupture (see Fig. 1).

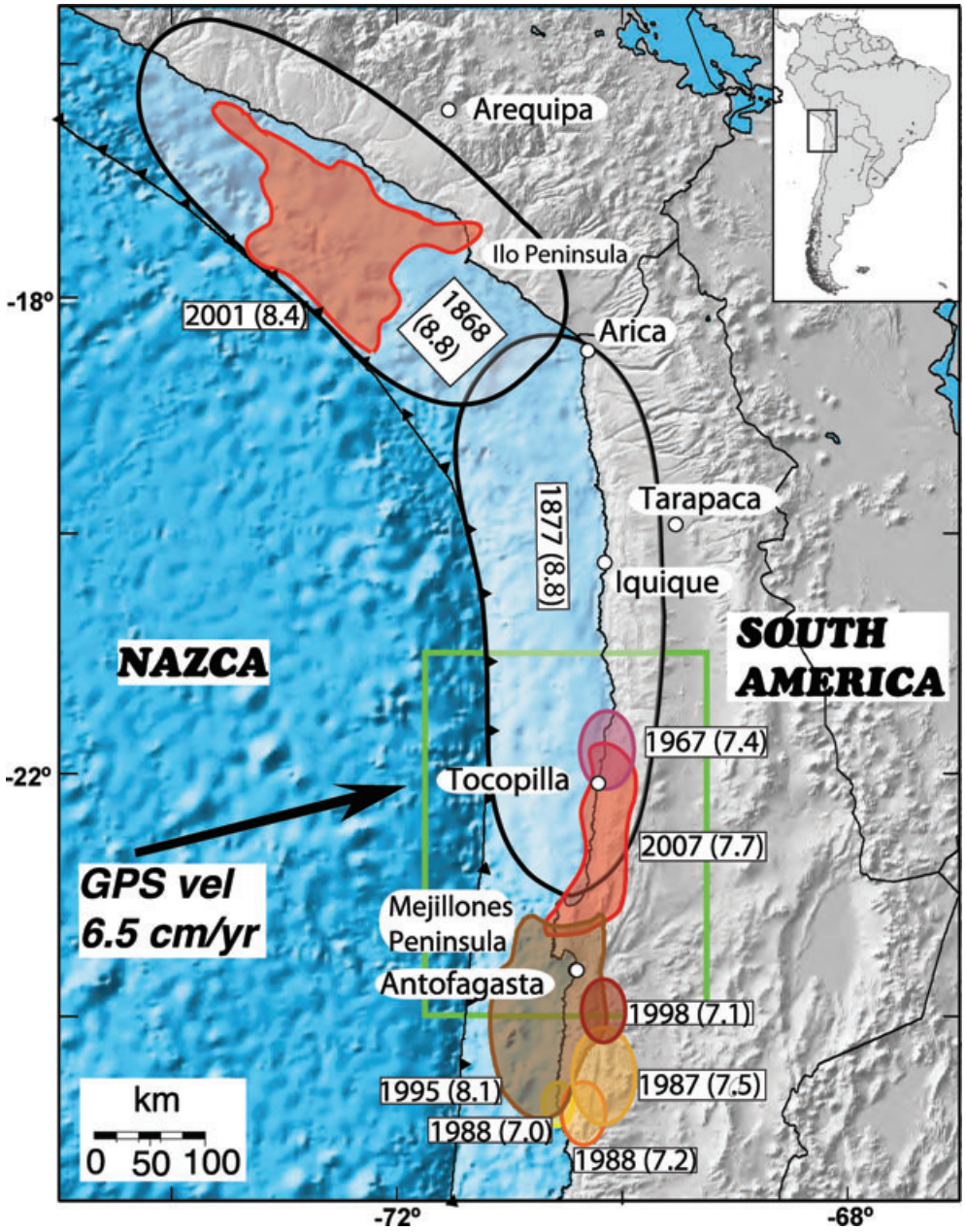

Figure 1. Reference map of our study area in northern Chile (delimited by a black box in the inset map). Rupture areas of historic and recent earthquakes are shown with their dates and magnitudes. Approximate ruptures areas of the two largest historic earthquakes in the region (the 1868 South Peru and the 1877 Iquique earthquakes) are represented as semi-transparent grey ellipses. Colour filled areas represent rupture areas of large instrumental shallow interplate thrust earthquakes. For those earthquakes with known distributed slip we use the outermost contour to represent the rupture area (for the 1995 earthquake from Chlieh *et al.* 2004, for the 2001 Arequipa earthquake from Pritchard *et al.* 2007 and for the 2007 earthquake from this work). Otherwise rupture area is represented by a coloured ellipse. The relative Nazca–South American convergence rate and direction are shown by the black arrow (Angermann *et al.* 1999) and the trench is shown by the black barbed line. The green box shows the region in Fig. 2.

3 DATA USED

3.1 InSAR data

We use 4 Envisat ASAR images from two descending tracks (track 96 and track 368, Fig. 3a) to form two independent coseismic interferograms. Both interferograms span the date of the earthquake and they include some days after the main shock: 10 d in the case of the track 368 interferogram and 26 d in the case of the track 96 interferogram. It is therefore probable that they include some post-seismic deformation together with the coseismic deformation. Data were processed using the Caltech/JPL (Pasadena, CA, USA) repeat-orbit interferometry package (ROI PAC, Rosen *et al.* 2004). We construct each interferogram by calculating the phase difference between two ASAR images using the two-pass approach (see Massonnet & Feigl 1998 for an overview of the method). The topographic phase contribution was removed using a 3-arc-s (90 m) digital elevation model from the Shuttle Radar Topography Mission (SRTM) (Farr & Kobrick 2000). The orbital information used in the processing was provided by the

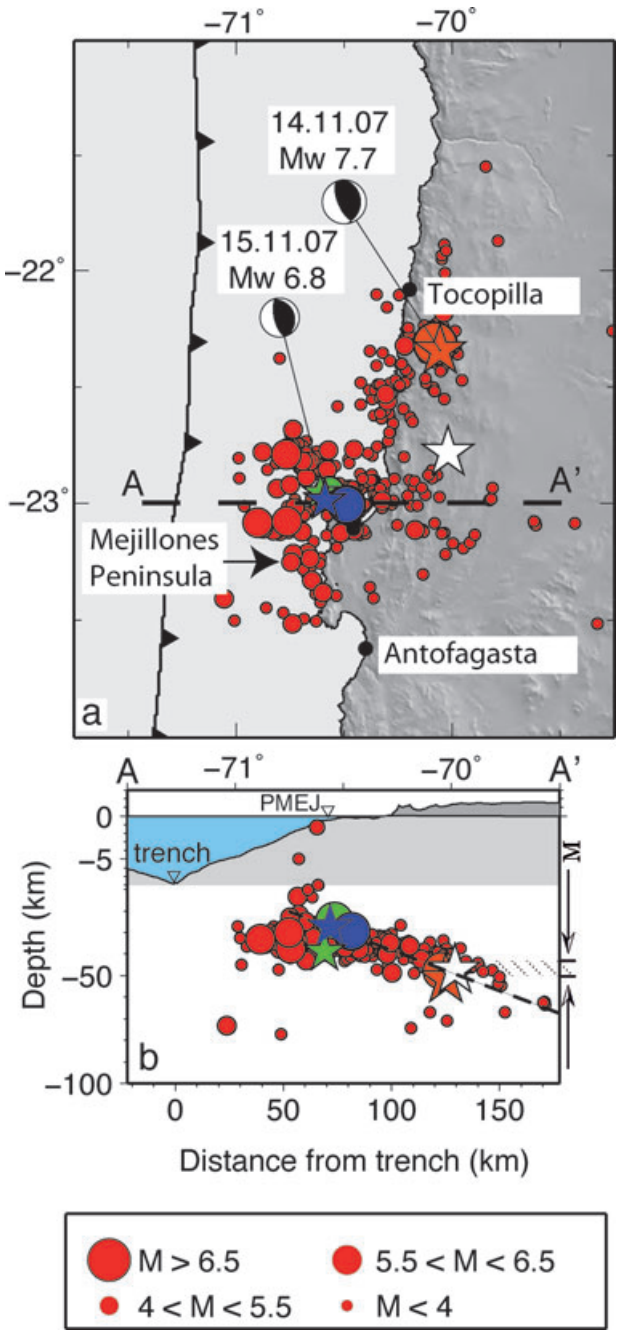

Figure 2. (a) Location of the Tocopilla main shock sources and aftershocks epicentres from 2007 November 14 to December 10. Circles correspond to epicentres located by the Seismological Service of Universidad de Chile. The size of the circles is proportional to the magnitude of the earthquakes. The epicentre of the main shock and the two large aftershocks occurred on 2007 November 15 (Mw 6.3 and Mw 6.8) are indicated by the orange, the green and the blue circles, respectively. Red circles represent other aftershocks. Stars denote epicentres localized by Peyrat *et al.* (2010) for the main shock (red star), a second subevent occurred south of the main shock ∼23 s later (white star) and the Mw > 6 aftershocks on 2007 November 15(green and blue stars). These authors combined teleseismic and strong motion data. Focal mechanisms of the main shock and the Mw 6.8 aftershock from same authors are also shown. (b) East–West seismicity cross-section at the latitude—23. 0°. Dashed black line represents the subduction interface deduced by the ANCORP seismic profile (ANCORP Working Group, 2003). Striped area represents depth interval where the continental Moho intersects the subduction interface (Patzwahl *et al.* 1999).

European Space Agency (DORIS orbits). Final results contain the relative displacement between the two dates in the radar line of sight (LOS) direction from ground to satellite, which is inclined ∼23° from the vertical, varying from 18° in the near range to 26° in the far range. Therefore, they are mostly sensitive to vertical displacements. The coherence of the interferograms is exceptionally high, because of the aridity of the Atacama Desert in northern Chile and the short time period in both interferograms (∼1 month).

Figs 3(b) and (c) show the observed displacements along the LOS direction for both unwrapped interferograms. The surface deformation pattern is characterized by two lobes: the western one shows a range decrease, corresponding to LOS displacement towards the satellite, with a maximum value of ∼30 cm; the eastern one represents a LOS displacement away from the satellite, with a maximum value of ∼15 cm.

InSAR data are affected by coherent noise primarily attributable to atmospheric and ionospheric effects (e.g. Hanssen 2001; Lohman & Simons 2005). Here we analyse the spatially correlated noise by calculating the power spectra of each interferogram as a function of the distance between pixels (e.g. Puysségur *et al.* 2007). We mask the deformation region to calculate the background noise and we search for the characteristic distance at which the spectrum reaches a stable maximum value: we pick up a distance value of 40 km for both interferograms. The interferograms are characterized by maximum noise value of 0.9 cm (2 rad) for track 368 and 0.35 cm (0.8 rad) for the track 96 (see Fig. A1 in the Appendix A). We observe some signals in the far field correlated with the topography, which might be due to variations of the content in tropospheric water vapour between acquisitions of radar images. In any case, the estimated level of noise is small compared to the deformation signal, and it should not affect much our InSAR measurements.

3.2 GPS data analysis

As our two interferograms include 10–26 d of post-seismic deformation following the Tocopilla earthquake, it is difficult to separate the deformation associated with Tocopilla main shock from the deformation generated by the largest aftershocks (Mw 6.3 and Mw 6.8, 2007 November 15) and by the post-seismic afterslip. To separate the contribution of the big aftershocks and the post-seismic afterslip to the superficial strain field, we use continuous GPS (cGPS) data acquired in the frame of a Chilean-French-USA cooperation. The North Chilean cGPS network includes 27 cGPS stations (between 18°S and 23.5°S) embedded in solid bedrock outcrops, reinforced concrete buildings or concrete benchmarks where sediments are unconsolidated. In this network, 11 cGPS stations distributed between the coast line (∼80 km east from the trench) and ∼300 km east from the trench in the continent (Fig. 3a) cover well the deformed zone identified with InSAR. We analyse coordinate time-series of the cGPS records from 30 d before to 26 d after the earthquake.

We use the GAMIT software (King & Bock 2000) to estimate daily station positions using 24-hr sessions data with 30 s of sampling frequency. We split the 24-hr session of the day of the earthquake into two sessions, excluding the hour during which the main shock has occurred, which is not considered in the calculation, to reduce uncertainties associated with surface seismic waves propagation. The same procedure is applied for the two Mw > 6 aftershocks of November 15, which occurred only 3 min apart and are calculated jointly (Fig. 3e). We set the ionosphere-free linear combination to perform ambiguity-free solutions. We use precise orbits and antennae phase centres tables from International GNSS Service for Geodynamics (IGS) (Beutler *et al.* 1993). For

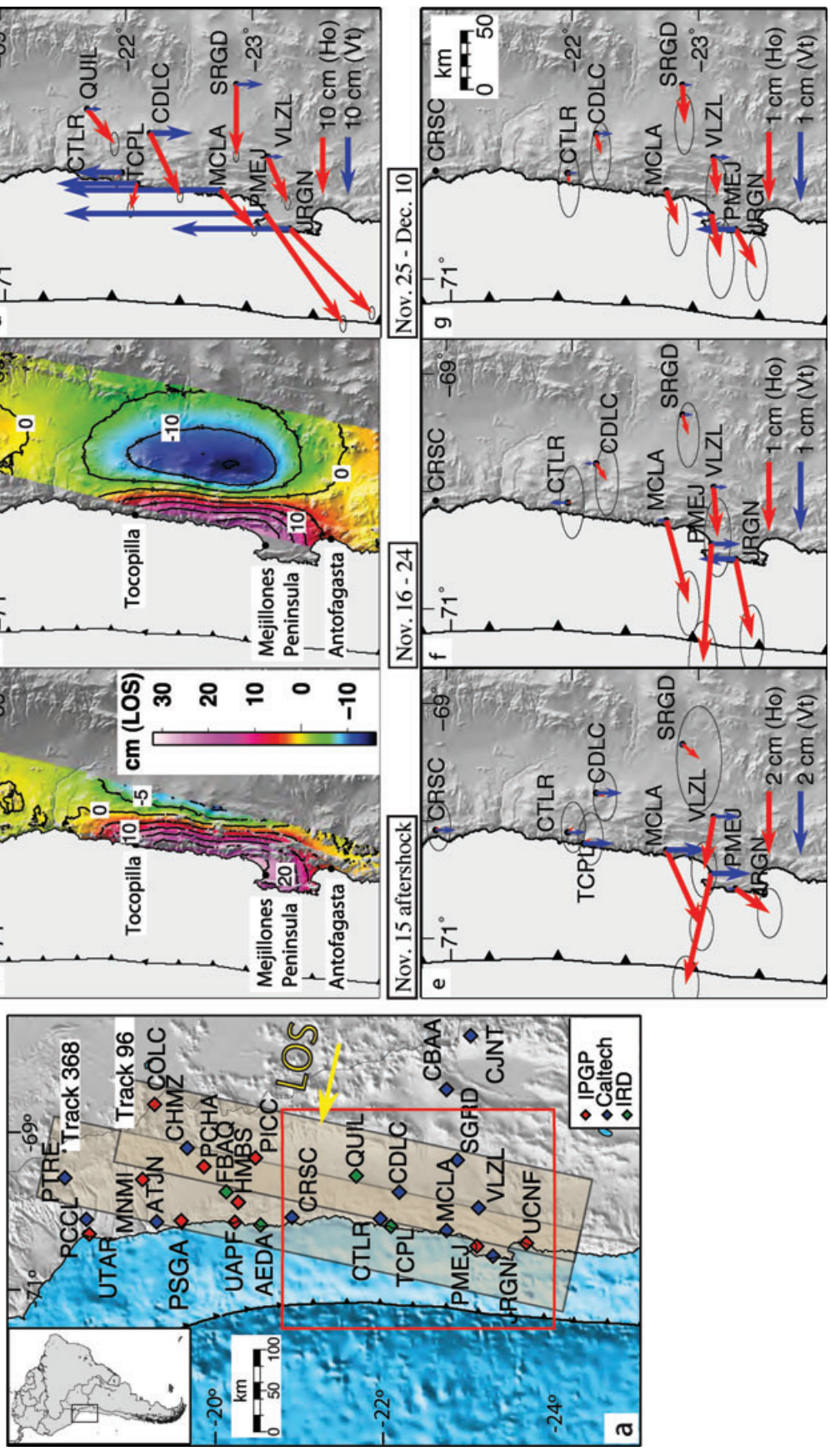

Figure 3. InSAR and cGPS data used in this study. (a) Reference map with the complete cGPS network in North Chile. Red, blue and green diamonds show positions of continuous GPS stations from IPGP, Caltech and IRD, respectively. Black rectangles delimit the extents of the radar scenes used in this study (track 368 and track 96). The satellite to ground radar line-of-sight (LOS) is shown with a yellow arrow. The red box shows the region covered in Figs (b)–(f). (b) and (c) Unwrapped interferograms showing surface displacement associated with 2007 November 14 Tocopilla earthquake. The two interferograms cover a 35 d period spanning the day of the earthquake. Track 368 interferogram (b) includes 10 d of post-seismic period (from 2007 October 10 to November 24) and track 96 interferogram (c) includes 24 d of post-seismic period (from 2007 November 5 to December 10). The colour scale refers to change in the radar line-of-sight (LOS) direction. Positive displacements are associated with a range decrease (movement towards the satellite). (d)–(g) Red arrows show the horizontal displacement and blue arrows show the vertical displacement in four different periods: (d) main shock coseismic displacements (cGPS-main), (e) displacement associated with the November 15 aftershock (cGPS-15aft), (f) first post-seismic period measured (cGPS-post1, from 2007 November 16 to November 24) and (g) second post-seismic period measured (cGPS-post2, from 2007 November 25 to December 10).

every station, one tropospheric vertical delay parameter per 4 hr is estimated. The baseline repeatability for pairs of stations less than 350 km apart are precise to within a millimetre in average (rms-north 0.9075 mm, rms-east 0.98825, rms-up 1.19475). Every daily and earthquake-session solutions include data from a selection of 13 permanent IGS stations located in South America, five of them on the tectonically stable craton (AREQ, BRAZ, BOGT, BRFT, CHPI, CFAG, CONZ, ISPA, LPGS, KOUR, SANT, UNSA and TUCU).

We combine these bias-free daily solutions using GLOBK Kalman filter software (Herring *et al.* 1990) through a regional stabilization procedure, solving for a translation, a rigid rotation and a scale factor of the reference frame at each epoch. The resulting reference frame comes from the minimization of the position and velocity values of well-determined fiducial stations around our study area from their *a priori* values. For the 30 daily solutions before the earthquake and the earthquake-session solutions a regional stabilization was calculated using IGS fiducial stations (BOGT, BRAZ, BRFT, CHPI, KOUR, LPGS, SANT and ISPA) determined in the International Terrestrial Reference Frame (ITRF) 2005 (Altamimi *et al.* 2007). For the 25 daily solutions after the large aftershocks on November 15 (from 2007November 16 to December 10) a local stabilization was calculated using five far field stations located away from the deformation zone (UTAR, COLC, PSGA, PICC and HMBS). These reference stations are located >100 km to the north of the deformation zone and no perturbation associated with the Tocopilla earthquake could be detected in the time-series. We assume that less than 1 mm of motion has occurred at the local reference stations during the 26 d after the main shock.

To estimate possible rapid afterslip deformation that might have occurred during the hours following the main shock, we calculate differential phase kinematic positions during 10 min before and after the main shock using TRACK software (Herring *et al.* 1990). We use data sampled at 15 and 30 s and precise orbits from IGS centre. The CRSC station located ∼120 km outside of the deformation zone was used as a fixed reference station. Linear combination ionospheric delay corrected phase was used to fix the ambiguities. We obtain an average of 40 000 double differences with 29.3 mm of average rms. Coseismic displacements estimates using kinematic (10 min before and after) and static (∼10 d before and after the earthquake) analyses are very similar and show no systematic difference. If some afterslip occurred during the hours following the main shock, its amount is small compared to some other earthquakes (such as the Sanriku-Oki in 1994 for example, Heki *et al.* 1997) and should have generated a maximum surface displacement of a few centimetres at our GPS stations, which is the order of magnitude of the uncertainty associated with the kinematic processing. Note that this represents the same order of magnitude that the horizontal displacements measured in coastal GPS stations during the post-seismic period, that could be detected thanks to a more precise static positioning (Table B3 in Appendix B). For similar reasons, rapid afterslip that might have occurred during the day of the two large aftershocks would also be undetectable. Hence, we cannot rule out the occurrence of rapid afterslip following the main shock and the large aftershocks. However, due to the detection threshold of kinematic positioning (a few centimetres), the amount of such rapid afterslip is necessarily limited and of the same (or smaller) order of magnitude that the post-seismic deformation that follows.

Hereafter, displacements calculated for the hour of the main shock are referred as cGPS-main, displacements calculated for the hour around the two Mw > 6 aftershocks are referred as cGPS-15aft, displacements occurred between 2007 November 16 and 24 are referred as cGPS-post1 and displacements occurred between 2007 November 25 and December 10 are referred as cGPS-post2. GPS vectors corresponding to these time intervals and time-series for the 11 stations within the deformation area are shown in Appendix B.

3.3 Comparison between data sets

InSAR and GPS measurements spanning the same time period can be directly compared when the GPS station lies inside the region covered by the interferogram. Out of 11 stations processed, six stations lie inside at least one interferogram track. The GPS vectors are projected into the direction defined by the radar LOS (see Appendix C, Table C1). Differences between measurements derived from GPS and from interferograms can be explained by orbital uncertainties in the SAR images (expressed by apparent 'offsets' and 'tilts' of the images). To correct for these tilts, we use the GPS data as a reference and we calculate a linear ramp and an offset (phase constant) for each interferogram. After removing these offsets and tilts, the difference between measurements derived from GPS and InSAR data is ∼1 cm for track 368 and 0.6 cm for track 96 [see rms(orig) and rms(corr) for each track in Table C1, Appendix C]. This difference is of the same order of magnitude than the characteristic noise of the interferograms.

As mentioned before, interferograms span different time periods and may thus contain different post-seismic deformation. We checked that no significant deformation occurred between both interferograms by processing the GPS data during both time spans (Figs 3f and g). The displacement in the period between days 9 and 26 after the main shock (that correspond to the acquisition date of the second image of the two interferograms; Fig. 3g) is less than 1 cm in all stations (this quantity is even reduced when projected in the LOS direction). We conclude that both interferograms record the same surface deformation.

4 MODELLING

To explain the pattern of deformation we try to reproduce it by modelling the earthquake as a dislocation in an elastic medium (Okada 1985). We first invert for the geometric parameters by assuming a uniform slip on a rectangular fault. In a second step, we apply a linear inversion technique to estimate the slip distribution on the determined fault.

We prepare the InSAR data for inversion by reducing the number of points without losing significant information. We subsample both interferograms taking into account the local gradient of LOS displacement (e.g. Lasserre *et al.* 2005). Only points with a minimum LOS displacement difference of 2 cm and a maximum distance of 7 km are kept. This decimation procedure reduced the number of phase samples in both interferograms to about 2000, preserving a high density of points in the near field, where strong LOS gradients occur (Fig. D1, Appendix D). This approach is simple but has the advantage that we do not need to make hypothesis about the location and geometry of the source. For a complete discussion about the InSAR data decimation method see Lohman & Simons (2005).

In the following models, we take into account the local LOS vector.

4.1 Uniform-slip models (geometry of the fault plane)

Several geometries have been proposed for the thrust interface between the Nazca and South American plates in North Chile, using

various sets of data (e.g. Pritchard *et al.* 2002; ANCORP Working Group 2003; Chlieh *et al.* 2004; Pritchard & Simons 2006; Hayes & Wald 2009; Hayes *et al.* 2009; Peyrat *et al.* 2010). Diverse techniques have been used, ranging from seismic imagery to distribution of seismicity, each one associated to specific errors. Overall, the published planes geometries differ by ∼10° in dip and ∼15 km in depth (Fig. E1, Appendix E). In particular geometries derived from seismic models highly depend on the chosen velocity model. We therefore attempt to invert the geometry using our InSAR and GPS data. Although this is also associated with intrinsic errors, in particular on the depth value due to the elastic half-space assumption (e.g. Cattin *et al.* 1999), it provides an independent estimation that we compare to previous studies.

We use an inversion procedure based on a least-square minimization algorithm developed by Tarantola & Valette (1982) which assumes uniform slip on a rectangular fault plane defined using nine parameters (strike, dip, rake, length, bottom and top depth, average slip and geographical coordinates of the plane, see Table 1 for details). Determining the nine mutually dependent parameters of the fault plane is a highly non-linear process. To reduce the non-linearity we use *a priori* information on the fault geometry to constrain some of the parameters. The strike of the fault plane is fixed at 5°N. This value is taken from the orientation of the trench at the surface (GTOPO30) at the latitude of Tocopilla rupture and it is consistent with published values for the strike of the fault plane (358° from Harvard CMT (Centroid Moment Tensor) solution; 0° from Delouis *et al.* 2009; 358° from Peyrat *et al.* 2010). We explore a series of different values for the following parameters: position, dip and updip limit of the fault plane. We vary the position of the fault plane (x_0 and y_0) in a region wide enough to include all the subduction geometries previously published (Fig. E1, Appendix E). For each position we test planes with dip values ranging from 16° to 30° and updip limit (h1) between 20 and 40 km. For each initial condition, we run the inversion leaving the other four parameters free (length, downdip limit h2, rake and average coseismic slip). The rms misfit is estimated for each run. For each data set (InSAR and GPS), among the 3000+ combinations computed, we select the 100 best models based on their rms value.

We invert GPS and InSAR data independently to avoid mixing data with different view geometry and different sensitivity to the fault plane parameters. We then compare the optimal parameters deduced from each type of data to fix the final model geometry. In the inversions of InSAR data both tracks are equally weighted.

Table 1 shows the parameters for the optimal model of each data set (GPS and InSAR) with its standard deviation. In most cases the resulting parameter values deduced from both data sets are consistent. For example, the estimated dip value is ∼21°, which is consistent with the one deduced from the Harvard CMT and ANCORP seismic profile. However, the rake value differs by ∼12 ° from both data set inversion. The InSAR-only estimation for the rake value is about 93° but, due to the LOS geometry, InSAR data are not very sensitive to the movement parallel to the trench, so they are unable to estimate the strike-slip component of the movement. The inferred rake from GPS-only inversion is ∼105° (slip azimuth ∼N50°E), which is collinear to the convergence azimuth in this region (Angermann *et al.* 1999), indicating that the oblique convergence between Nazca and South America plates is most probably accommodated by an oblique slip vector on the subduction plane rather than by a slip partitioning as described in other regions (e.g. Sumatra, Fitch 1972). Figure E2 in the Appendix E shows the uncertainties analysis in form of histograms for each parameter for each data set.

To refine the most probable location of the fault plane (x_0 and y_0) we compute the spatial density of the 100 best-fitting fault planes in cross-section. We divide the cross-section in a grid of 5 × 5 km and count the number of planes that cross each patch. Our results are shown in Fig. 4. Red to black regions represent the preferred location of the fault plane. The light green line represents the fault geometry deduced from our data, that will be used for the slip distributed models. It is generally consistent with subduction interface geometries proposed in this region, although it is situated at a vertical distance of ∼10 km or more of some of them (e.g. Hayes & Wald 2009 plane, Peyrat *et al.* 2010 plane, CMT plane in Fig. E1, Appendix E). Our geometry requires the slope of the subduction interface to decrease towards the west to reach the ocean floor at the trench and is consistent with the change in dip deduced from seismic refraction experiments in this region (dip between 9° and 25°, Patzwahl *et al.* 1999). This change in dip of the subduction interface was already suggested for the 1995 Antofagasta earthquake rupture plane from the inversion of GPS data (Ruegg *et al.* 1996) and from waveform inversion and aftershocks distribution (Delouis *et al.* 1997). The parameters of the preferred model are indicated in the last row of Table 1.

Our preferred model produces a first-order fit to the observed deformation pattern (Fig. E3, Appendix E). However, the observed GPS and InSAR displacements are poorly fit in the southern half of the rupture, arguing that the slip distribution is not spatially constant. Therefore models that allow for spatial slip variations along the fault plane are required.

4.2 Distributed-slip models

4.2.1 Modelling strategy

We extend the fault plane previously determined along strike and downdip and we divide it into an array of 19 × 12 elements, each measuring ∼14 km × 14 km. To solve for the slip distribution along these 228 patches we use a least-squares minimization with the non-negativity constraint on the slip. We impose the rake of 105° inferred from the uniform slip modelling. To limit oscillations of the solution, we impose some smoothing on the solution, by minimizing the second-order derivative of the fault slip (e.g. Harris & Segall 1987; Du *et al.* 1992; Arnadottir & Segall 1994; Grandin *et al.* 2009).

Table 1. Source parameters for each data set and the preferred model (see Section 4.1 for details). Values of dip, rake, longitude and latitude are in degrees, slip is in metres and all other parameters are in kilometres. Long and Lat refers to the location of the centre of the upper part of the fault plane projected diagonally to the surface. Longitude and latitude values for the preferred model are deduced from the density plot analysis (Fig. 4).

Data set	Dip	Rake	Length	h1	h2	Slip	Long	Lat
GPS	22 ± 3	105 ± 2	152 ±5	32 ± 5	53 ± 4	1.32 ± 0.2	−71.21 ± 0.18	−22.58 ± 0.05
InSAR	20 ± 3	93 ± 2	155 ± 8	29 ± 6	48 ± 6	1.2 ± 0.17	−71.25 ± 0.17	−22.52 ± 0.05
Preferred	20	105	156	26	47	1.1	−71.158	−22.55

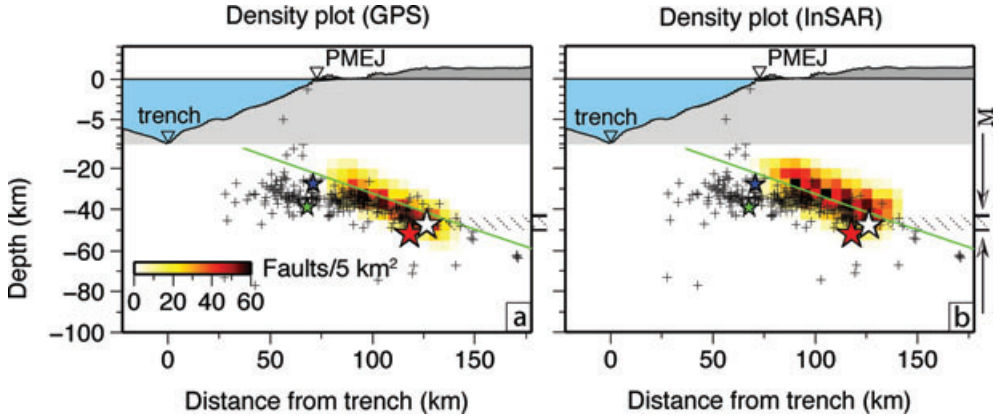

Figure 4. Density plots of the set of 100 best-fitting fault planes for the 2007 main shock from (a) GPS data inversion and (b) InSAR data inversion. The planes are projected in a cross-section perpendicular to the fault strike (5°) at latitude—23.0°. The colour scale represents number of faults plane that passes through each 5 km × 5 km patch. Light green line represents fault interface deduced from this study. The black crosses are aftershocks located by the Seismological Service of Universidad de Chile (correspond to red circles in Fig. 2). Conventions for the main shock and large aftershocks located by Peyrat *et al.* (2010) (coloured stars) are the same as in Fig. 2.

We perform independent inversions of each data set as well as joint inversions. As we previously verified that both tracks basically contain the same LOS deformation, we invert them jointly (InSAR-only inversion). We perform a joint inversion including both InSAR tracks and cGPS data spanning 10 d after the earthquake, thus containing a similar amount of post-seismic deformation than the interferograms. For the joint inversion of the InSAR and cGPS data we experiment with different weighting. We search for a compromise between the rms (that should be similar in both data sets) and the spatial density of each type of data.

We determine the optimal solution roughness that will be used in our final models searching for a compromise between the roughness and the misfit of the solution (e.g. Menke 1989; Jonsson *et al.* 2002). For all the coseismic models we apply the same roughness, determined from the trade-off curve of the joint model (Fig. F1a, Appendix F). For the post-seismic and aftershock models, however, we cannot apply the same smoothness as each of them present a very different value of average slip on the fault patches and this yields very different roughness values (see eq. 5 in Jonsson *et al.* 2002). Therefore, we determine the optimal value from the trade-off between misfit and solution roughness of each data set (Figs F1b–d, Appendix F). We pick the optimal roughness values indicated by arrows in Fig. F1 for our final solutions, as lower roughness result in worse misfit but higher roughness does not improve the misfit much (though the slip distribution does not significantly vary for modest changes in roughness).

4.2.2 *Resolution of the distributed slip models*

We examine the spatial resolution of our distributed slip models through various checkerboard tests. To evaluate the capacity of each data set to solve for the slip distribution on the fault plane, we first construct a model using the same plane as in our distributed slip inversions using a patch size of ∼40 km × 40 km. Following a checkerboard design we assign each patch 0 or 1 m of slip (Fig. G1a, Appendix G). The surface deformation due to this model is then computed at all the locations where we have GPS and InSAR observations. These simulated data sets are inverted for distributed slip using the procedure described above. Figs G1(b)–(d) show the results of the inversions using each type of data separately and jointly (see an alternative checkerboard test in Fig. G2, Appendix G). The lower spatial resolution of GPS inversion compared to InSAR inversions is obvious, as expected due the different data coverage (666 and 904 InSAR points in track 368 and track 96 interferograms, respectively, while only 11 3-D GPS displacements are available). All data sets solve better for the slip patches located directly at depth, while regions where data coverage is poor or non-existent (e.g. at sea) have a worse resolution. Despite the limited coverage of cGPS data, they solve reasonably well for the slip patches located below land, because they are equally distributed on land, but the spatial resolution offshore is significantly degraded. In the case of InSAR data, both tracks constrain the slip distribution model equally well below land, while the patches below sea are better resolved by track 368 data, that covers the coast and the Mejillones Peninsula. When we invert all data sets jointly, using the same weight as in our distributed slip models, the spatial resolution is reduced comparing to InSAR data but improved compared to GPS-only inversion.

4.2.3 *Results*

Fig. 5 shows three coseismic slip distributions from two different data sets inverted independently and jointly. Only the first one corresponds to the purely coseismic interval, the other two include 10–26 d after the main shock. Table 2 shows the main characteristics of these models.

All the models present two main areas where the slip reaches a maximum, which are interpreted as asperities (assuming that asperities are regions on the fault plane with higher values for coseismic slip and moment release than their adjacent areas, e.g. Lay & Kanamori 1981). The northern one has a very similar location in all the models except for the GPS-only inversion, where this asperity is centred slightly south of same asperity in other models. This different location may be due to the lower resolution of the GPS-only inversions compared to the InSAR-only and joint inversions. This northern patch is located between 30 and 50 km in all the inversions and presents an elongated shape to the north.

The southern asperity seems to be located below the northern half of the Mejillones Peninsula in all models and does not extend into its southern part. However, the southern asperity seems to extend to shallower depth in the two inversions including deformation during

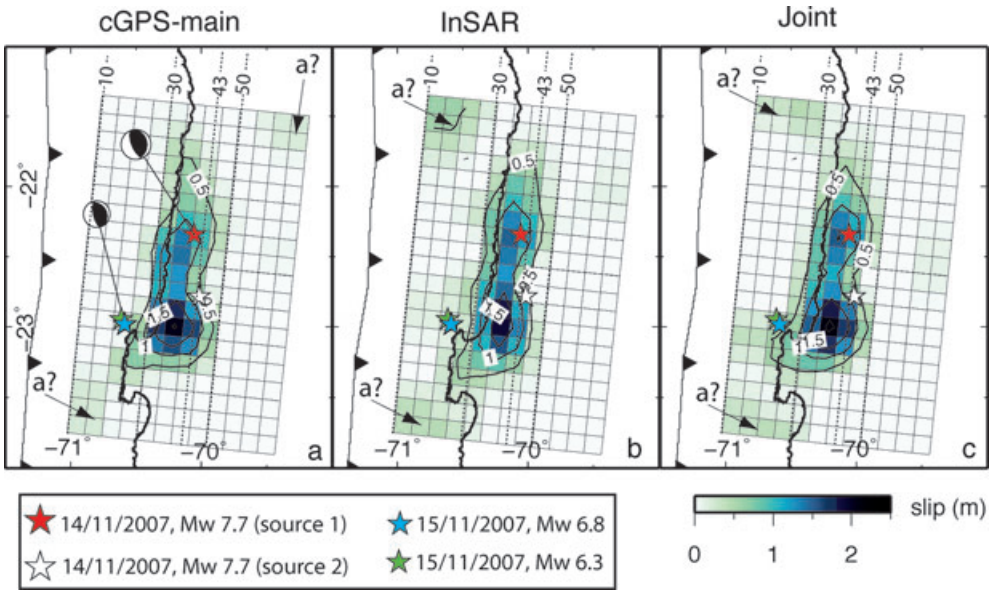

Figure 5. Distributed slip models for the Tocopilla earthquake using different data sets. (a) Slip distribution inverted from coseismic cGPS data. (b) Slip distribution from InSAR data. (c) Joint GPS-InSAR inversion. GPS in this case includes 26 d of post-seismic deformation to span a period comparable to InSAR. Colours and contours (0.5 m interval) show the magnitude of slip in metres. Slip patches labelled with 'a?' are probably artefacts due to resolution problems (see text for details). The Peyrat *et al.* (2010) locations for the main shock and largest aftershock are shown as stars. Depths on the fault interface are shown as black dotted lines labelled at top. The depth interval where the continental Moho intersects the subduction interface is 43–50 km (Patzwahl *et al.* 1999). See Table 2 for details on each model.

some days after the main shock, especially in the joint inversion. In this region, the largest aftershocks (*M*w 6.3 and *M*w 6.8) occurred on November 15 during the time span covered by the data. The maximum depth of this southern asperity is also 50 km in all the inversions. Residuals and rms corresponding to these coseismic models are shown in Fig. H1 (Appendix H).

The slip distribution corresponding to the surface displacement that occurred on 2007 November 15 is shown in Fig. 6(a). Most of the slip is concentrated in a patch NW of the Mejillones Peninsula (labelled 1 in Fig. 6a), which are coincident with the hypocentres of the two large aftershocks that occurred on 2007 November 15. This southern patch seems to reach a shallower depth (less than 10 km) and its bottom is at 30 km depth. There is another little patch (2 in Fig. 6a) between 25 and 30 km depth, north of the main one. The residuals corresponding to this model are shown in Fig. H2(a) (Appendix H).

Finally, the slip distribution models corresponding to the two post-seismic periods studied (data cGPS-post1 and cGPS-post2) are shown in Figs 6(b) and (c) and their residuals in Figs H2(b) and (c). The model for the first period of post-seismic deformation (2007 November 16–24), which is the closest to the main shock, shows less slip (up to 22 cm) than that associated with the November 15 aftershocks, but with a very similar location (patch labelled 3 in Fig. 6b). Another patch with less that 2 cm of slip is located between the two main shock sources (4 in Fig. 6b). The model corresponding to the second post-seismic period, which starts 10 d after the main shock (associated with too subtle deformation to be recorded in the interferograms, as discussed earlier), shows a patch of up to 2 cm of slip concentrated between 20 and 35 km depth, centred beneath the NW part of the Mejillones Peninsula (patch labelled 5 in Fig. 6c).

As we discuss in the previous section, the resolution of our inverted slip model is poor near the edges of the modelled fault plane that are far from our observations (e.g. southwestern and northwestern corner of the fault plane). Therefore, the patches labelled with 'a?' in Fig. 5 and Fig. 6 are probably artefacts caused by poor resolution.

Table 2. Some characteristics of the models in Figs 5 and 6.

		cGPS-main	InSAR	Joint	cGPS-15aft	cGPS-post1	cGPS-post2
Complete model	S-M0 (N m)	3.18E + 20[a]	–	–	2.4E + 19[b]	4.45E + 18[c]	4.12E + 17[c]
	G-M0 (N m)	2.90E + 20	3.68E + 20	3.18E + 20	1.99E + 19	1.43E + 19	7.47E + 18
	Top (km)	30	30	30	<10	<10	<10
	Bottom (km)	50	50	50	30	40	45
Patch N	M0	1.26E + 20	1.44E + 20	1.31E + 20	6.2418E + 17	–	–
	Top (km)	30	30	30	25		
	Bottom (km)	50	50	50	30		
Patch S	M0	1.64E + 20	1.63E + 20	1.87E + 20	1.93E + 19		
	Top (km)	25	25	10	<10		
	Bottom (km)	50	50	50	30		

Notes. [a]Seismic moment for the main shock (Peyrat *et al.* 2010). [b]Cumulative seismic moment for the *M*w 6.8 and *M*w 6.3 2007 November 15 aftershocks (Neic catalogue). [c]Cumulative seismic moment for aftershocks occurring during each post-seismic period studied (Section 4.2.3).

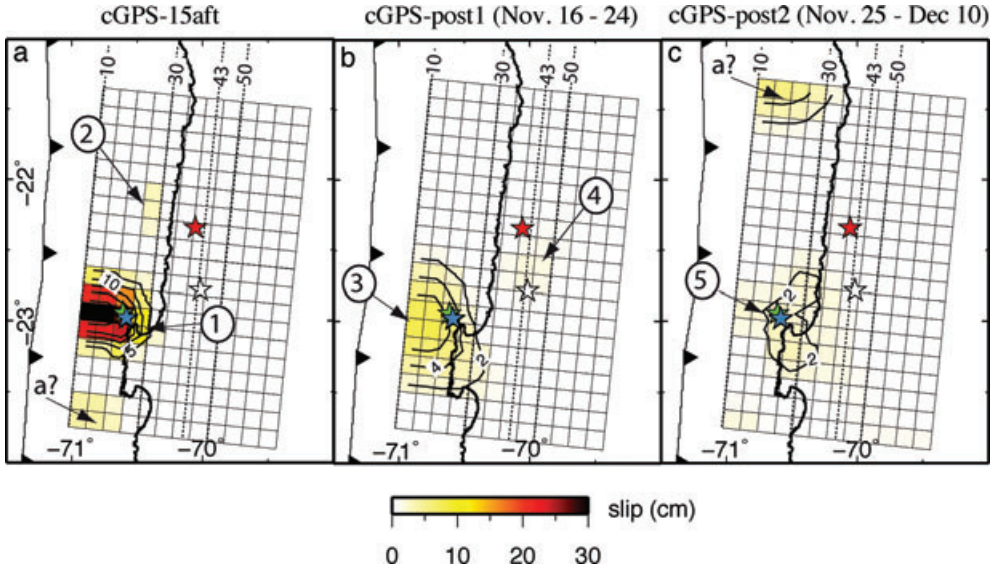

Figure 6. Slip distribution inverted from GPS data for (a) the largest aftershocks (2007 November 15), (b) 9 d of post-seismic deformation (2007 November 16 to November 24) and (c) 16 d of post-seismic deformation (2007 November 25 to December 10). The time interval of (b) corresponds to the post-seismic interval included in the track 368 interferogram and the temporal span of (b) plus (c) (2007 November 16 to December 10) correspond to the post-seismic interval included in the track 96 interferogram. Contours of slip [5 cm interval in (a) and 2 cm in (b) and (c)] are superimposed with a colour scale. Conventions are the same as in Fig. 5. See Table 2 for details on each model.

To determine whether this post-seismic afterslip is aseismic, such as slow slip events, or a seismic process, we compare the geodetic moment release estimated for the two post-seismic periods with the cumulative moment release of aftershocks during the same time intervals. To estimate the moment released by the aftershocks we use local magnitudes provided by the regional network (DGF) and the worldwide network data for 16 events of Mw > 5 published in the NEIC catalogue to calculate an empirical relationship between Ml and log Mo. According to the obtained empirical law (log Mo = 1.5841Ml + 9), the aftershocks that occurred between 2007 November 16 and 24 released a cumulative moment of 4.4501×10^{18} N m, representing 30 per cent of the geodetic (GPS) moment in our model for the same period. Similarly, the cumulative moment released by aftershocks that occurred from 2007 November 25 to December 10 is 4.12×10^{17} N m, and represent 5 per cent only of the geodetic moment released for the same period in our model. This suggests that 70 per cent of the post-seismic deformation during the first post-seismic period (2007 November 16–24) and 95 per cent of that during the second post-seismic period (from 2007 November 25 to December 10) correspond to aseismic slip in the subduction interface. Although our estimate of the cumulative moment is rough (waiting for results of more accurate seismological studies to come), the implication of significant aseismic slip associated with the post-seismic deformation appears robust.

5 DISCUSSION

Our preferred models for the Tocopilla main shock show slip concentrated in two main asperities (Fig. 5), consistent with previous seismological data (Delouis *et al.* 2009; Peyrat *et al.* 2010). These asperities are located between 30 and 50 km depth, suggesting that the shallow part of the seismogenic interface (from the trench to 30 km depth) remains unbroken with the exception of the southern edge of the rupture, at the latitude of the Mejillones Peninsula, where coseismic slip seems to have propagated up to ∼25 km depth. The coseismic rupture extends between the subduction interface beneath the region of the city of Tocopilla to the north and the region of the subduction interface beneath the Mejillones Peninsula to the south, already identified as an important intersegment zone (e.g. Ruegg *et al.* 1996). The slip associated with the Mw 6.8 and Mw 6.3 aftershocks is concentrated updip the southern end of the main shock rupture (Figs 5 and 6). Our analysis of the post-seismic deformation observed from 2 to 26 d following the 2007 Tocopilla earthquake suggests that most of the post-seismic deformation recorded by GPS occurs during the first post-seismic period measured (from 2007 November 16 to 24). It is concentrated updip the southern termination of the rupture, and well correlated with the aftershocks distribution for the same period. The overall post-seismic deformation occurring in this period represents a 5 per cent of the coseismic deformation and ∼70 per cent of this post-seismic deformation seems to have been accommodated as aseismic afterslip at the subduction interface. Nevertheless, due to the lack of resolution of kinematic GPS positioning, a threshold exists below which we cannot solve for a limited amount of rapid afterslip that could have occurred the day of the main shock and the day of the two large aftershocks. Hence, we cannot exclude that the rapid afterslip that might have occurred during these 2 d equals the post-seismic deformation produced during the following month (see Section 3.2). This would be consistent with the rapid deceleration that characterizes post-seismic relaxation governed by afterslip mechanisms (e.g. Marone *et al.* 1991; Çakir *et al.* 2003; Perfettini & Avouac 2004). Therefore, in the 10 first days following the main shock, aseismic slip might have increased by up to 10 per cent the moment released seismically by the main shock and large aftershocks. The amount of afterslip (14–22 per cent of the main shock seismic moment, including both seismic and aseismic creep) following the Tocopilla earthquake (from 2007 November 14 to December 10) is low compared to other subduction earthquakes of similar magnitude that occurred in other regions. This estimate of the afterslip only covers the first 26 d after the earthquake, but this seems to include the major part of post-seismic deformation if one considers a logarithmic decrease of the

amount of post-seismic slip. A sudden acceleration of aseismic slip that would occur later could not be directly related to post-seismic afterslip *sensus stricto* but rather to a slow slip event that might be triggered by an increase of coulomb stress in the area. For example, the Mw = 7.7 1994 Sanriku-Oki (Japan) and the Mw = 7.8 1997 Kamchatka earthquakes were followed by post-seismic afterslip increasing the coseismic moment by 100 per cent in 1 yr in the case of the Japan earthquake (Heki *et al.* 1997) and 2 months in the case of the Kamchatka earthquake (Bürgmann *et al.* 2001). However, the percentage of afterslip following Tocopilla earthquake is comparable with nearby events, like the Mw 7.7 1996 Peru and the Mw 8.1 1995 Antofagasta earthquakes that also seem to have released little post-seismic deformation (<10 per cent of coseismic moment after first 60 d for Peru earthquake, Pritchard 2003; between 10–20 per cent of the coseismic moment in the case of Antofagasta in 3 yr, Chlieh *et al.* 2004; Pritchard & Simons 2006). In the same subduction zone, however, significant afterslip followed the Arequipa 2001 Mw 8.4 earthquake in South Peru (afterslip equivalent to 20–40 per cent of the coseismic moment in 1 yr, Ruegg *et al.* 2001; Melbourne *et al.* 2002; Pritchard 2003).

These results raise specific questions. Why the Tocopilla rupture does not break the subduction interface up to the trench? What barriers inhibited updip and downdip propagation of the rupture? What barriers stopped the lateral propagation of the rupture (north and south)? Why did the earthquake nucleate at the latitude of Tocopilla? Can we image areas with different slip behaviour? How does the afterslip distribution compare to the Tocopilla main shock slip distribution and to other earthquakes in this region? What is the amount of slip deficit remaining after Tocopilla earthquake?

5.1 Our results in relation to the downdip and updip terminations of the rupture

The downdip limit of the Tocopilla rupture (50 km) is consistent with the bottom edge of the seismically coupled interface defined from background seismicity and focal mechanisms in this region (Tichelaar & Ruff 1991; Suarez & Comte 1993; Comte & Suárez 1995; Delouis *et al.* 1996) and with the downdip extent of the fully or partially locked fault zone as deduced from geodetic measurements of interseismic strain here (Bevis *et al.* 2001; Khazaradze & Klotz 2003; Chlieh *et al.* 2004). The maximum depth of the 2007 rupture seems to correlate with the depth range where the continental Moho intersects the subduction interface, between 43–50 km in this region (Patzwahl *et al.* 1999, see striped region in Figs 2, 4 and 7). The intersection of the subduction plane with the continental forearc Moho was proposed by Oleskevich *et al.* (1999) as the downdip limit of great subduction thrust earthquakes in subduction zones of old oceanic plates such as North Chile. These authors explained the stable-sliding behaviour of the thrust interface in contact with the mantle as a consequence of hydrated rocks (as serpentine or talc) present in the forearc metasomatized mantle. Our results support the idea that the mechanism controlling the depth extent of seismic coupling in the Tocopilla region is the depth of the continental Moho at the subduction interface, as previously suggested by several authors (Tichelaar & Ruff 1991; Delouis *et al.* 1996; Patzwahl *et al.* 1999; Chlieh *et al.* 2004).

A more challenging question is to understand why did the rupture not propagate into the shallow seismogenic zone (10–30 km). In this region interseismic strain has been accumulating since 130 yr and geodetic studies suggest that the shallower part of the subduction interface is locked (Bevis *et al.* 2001; Khazaradze & Klotz 2003; Chlieh *et al.* 2004). The occurrence of large tsunamigenic earthquakes, such as Mw 8.8 earthquake in 1877 and probably other large earthquakes before (Vargas *et al.* 2005), also pleads for a coupling of the shallow part of the seismogenic zone. However, for some reason the Tocopilla rupture was stopped at 30 km depth. Does this suggest the existence of a geometric barrier or a change in the frictional properties of the seismogenic interface at this depth that avoids the propagation of the rupture updip?

A change in the dip of the fault plane at ∼25–30 km depth could explain the updip limit of the rupture, as it may act as a geometric barrier to inhibit the propagation of the earthquake (e.g. Aki 1979; King 1986). Such a local bend of the subduction interface was imaged at that depth by seismic profiles at the latitude S21° (Patzwahl *et al.* 1999; ANCORP Working Group, 2003) and might be explained by the recent (<2 Ma) subduction of a 400 km width oceanic plateau, the Iquique Ridge (Rosenbaum *et al.* 2005). Though we assume for our models a simple geometry with no variations in dip, we already discussed in Section 4.1 that our modelled fault plane requires the subduction interface to decrease the dip by ∼5° towards the west to reach the trench, which is compatible with geophysical data. This change in dip was also suggested in the region offshore the city of Antofagasta, south of the Mejillones Peninsula (Ruegg *et al.* 1996; Delouis *et al.* 1997; Chlieh *et al.* 2004) and proposed by Armijo & Thiele (1990) to explain the formation of the Coastal Scarp of Northern Chile. These authors suggest that this geomorphic feature could be a large-scale west-dipping normal fault extending down to the subduction, created as a response to a change in dip at the subduction interface that would generate E–W extension within the upper plate. As the Coastal Scarp and the updip limit of the Tocopilla rupture are almost vertically aligned, the same structure could be controlling both phenomena. A complementary way to explain the updip limit of the rupture could be to regard it as the result of a change in the frictional properties between the upper (∼10–30 km depth) and the lower (∼30–50 km depth) seismogenic zone. Both kinds of changes (frictional properties and/or geometry) along the plate interface may explain an updip limit for moderate-to-large earthquakes in this region and our data do not exclude either of them, although geophysical observations rather support the first hypothesis (ANCORP Working Group, 2003). Such a change in the subduction interface is probably capable of arresting the rupture of moderate-to-large earthquakes that nucleate downdip, but it seems unlikely that it stops the rupture of great earthquakes nucleated on the shallow seismogenic interface and that may propagate down to the base of the locked interface zone (∼50 km) as it was observed for the 1995 Antofagasta earthquake (Ruegg *et al.* 1996; Ihmlé & Ruegg 1997; Klotz *et al.* 1999; Chlieh *et al.* 2004; Pritchard & Simons 2006).

5.2 Our results in relation to the lateral termination of the rupture (northern and southern limits)

The northern limit of the Tocopilla rupture in our models (Fig. 5) locates south of the zone previously ruptured by a Mw 7.4 in 1967 (Malgrange & Madariaga 1983; Tichelaar & Ruff 1991, see Fig. 1). According to kinematic models (Delouis *et al.* 2009; Peyrat *et al.* 2010), the Tocopilla main shock initiated in this region, suggesting a causal relationship between both events. The 1967 earthquake has most probably partially released stress accumulated in the interseismic period within its rupture zone, and loaded the adjacent segments towards both the north and the south, easing the nucleation of Tocopilla earthquake. Other authors suggest the structures

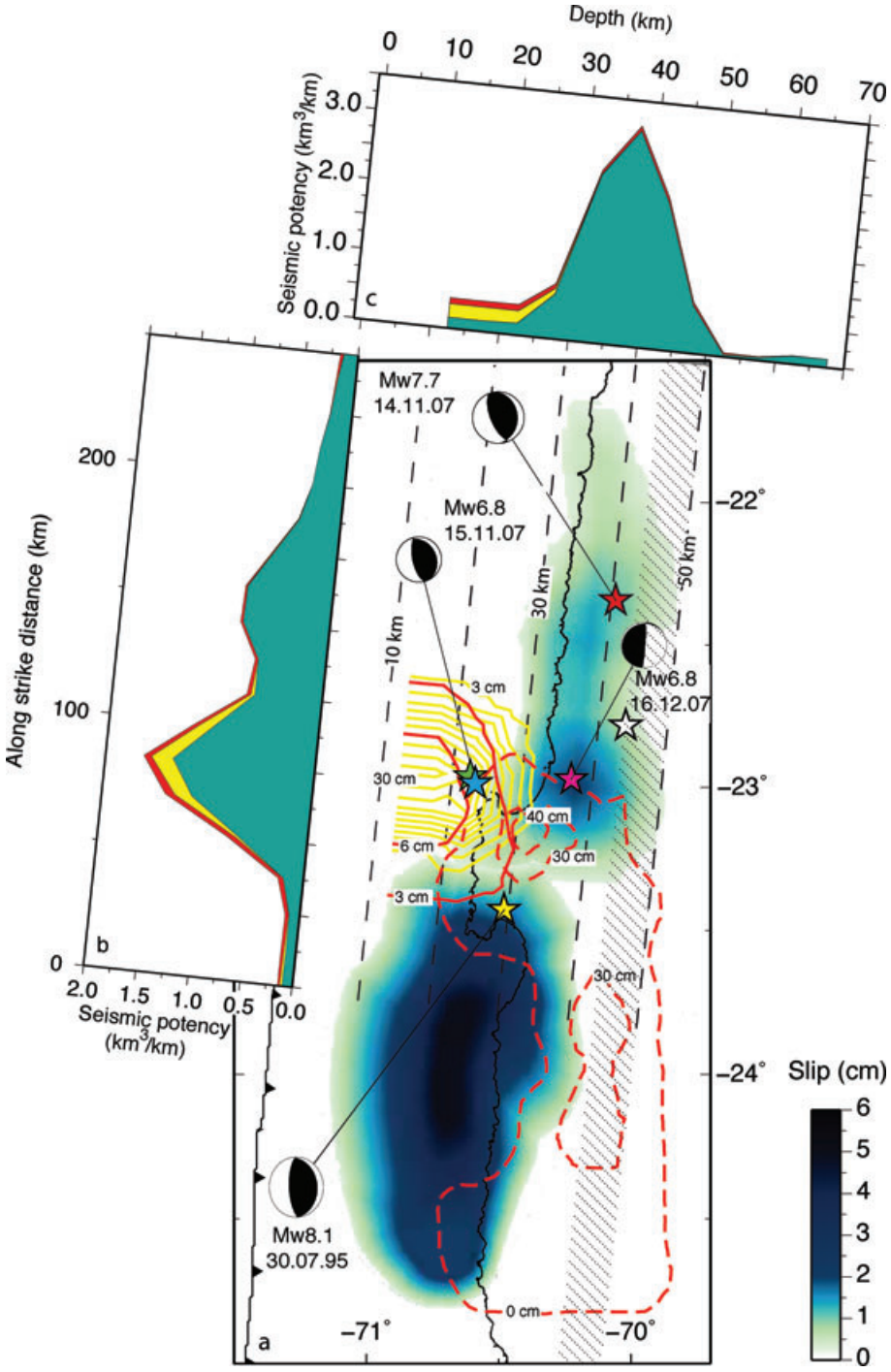

Figure 7. Comparison between the coseismic and post-seismic slip from the 1995 *M*w 8.1 Antofagasta and 2007 *M*w 7.7 Tocopilla earthquakes. (a) Magnitude of coseismic slip on the fault interface is represented by the colour palette for the 1995 and the 2007 earthquakes. Yellow and red solid contours represent slip distribution for the two large aftershocks and the first post-seismic period studied (cGPS-post1) following the Tocopilla earthquake, respectively. Contour interval is 3 cm in both cases. Red dashed contours (10-cm interval) represent 5-yr aseismic post-seismic deformation that followed the 1995 Antofagasta earthquake. Epicentre for both subevents of the main shock (red and white stars) and three large aftershocks (blue, green and pink star) and their focal mechanism from Peryat *et al.* (2010) are indicated. Epicentre (yellow star) and focal mechanism for the 1995 Antofagasta earthquake (from Monfret *et al.* 1995 and the Harvard CMT solution, respectively) are also indicated. (b) and (c) Seismic potency (product of ruptured area and slip) per kilometre along strike and along dip, for the coseismic (green area), November 15 aftershock (yellow area) and post-seismic (red area) models associated with the 2007 Tocopilla earthquake. The total geodetic moment for this model can be determined by summing the potencies and multiplying the sum by the value of the shear modulus of the Earth's crust (assuming an averaged shear modulus of 33 GPa moment values are those indicated in Table 2). Depths on the fault interface are shown as black dotted lines labelled every 20 km. The depth interval where the continental Moho intersects the subduction interface is shown as a striped area (Patzwahl *et al.* 1999).

in the upper plate (the Rio Loa faults) may control the initiation of the rupture in this area (Loveless *et al.* 2009).

The southern limit of the Tocopilla rupture beneath the Mejillones Peninsula underlies again the role of barrier of structures under this geomorphic feature, which coincides with the southern limit of the Iquique ridge that entered in subduction 1 or 2 Ma ago (Rosenbaum *et al.* 2005). According to our model of the first month of post-seismic deformation, seismic slip associated with the aftershocks (mostly to the *M*w 6.8 aftershock) and aseismic afterslip in the first 10 d after the main shock appear to have released a small part of the slip deficit in the shallow seismogenic zone at the latitude of the Mejillones Peninsula, and might be related to the specific barrier behaviour of this area.

Deformation associated with the 1995 Antofagasta earthquake bears some similarities with deformation in 2007. Fig. 7 shows those slip distributions overlain. The 1995 main shock coseismic slip was arrested under the southern part of the Mejillones Peninsula, not reaching its northern part. The post-seismic deformation during the 3 yr after the 1995 main shock (red dashed line in Fig. 7) propagated under the northern part of Mejillones Peninsula, and particularly to shallower depth. Most of the aftershocks of the 1995 Antofagasta earthquake and most of the afterslip were located to the northeast of the rupture (Chlieh *et al.* 2004; Pritchard & Simons 2006). Therefore both seismic and aseismic post-seismic deformation seem to occur in the region beneath the Mejillones Peninsula and its continuation updip. This suggests a complex frictional behaviour allowing for unstable sliding areas generating earthquakes in some places (asperities characterized by velocity weakening behaviour) and stable or conditionally stable zones (velocity hardening) promoting pulses of aseismic slip. These along strike variations in the seismogenic behaviour could be controlled by geological variation in the frictional parameters (Song & Simons 2003). However, given the distance between the subduction plane and the surface (20–40 km), geodetic data cannot resolve precise mapping of small sized asperities (a few square kilometres) versus zones of creep.

Earlier studies suggest that the structural singularity in the area of the Mejillones Peninsula, which is cut by large normal faults (Armijo & Thiele 1990) that might reach the subduction zone at depth (see distribution of aftershock seismicity) and might reflect structural complexity at depth (Armijo & Thiele 1990; Ruegg *et al.* 1996). For simplicity, in our models we assume a rectangular fault plane that does not vary where it reaches the Mejillones Peninsula. However the change in the slip distribution of the region beneath the peninsula, during the post-seismic period after the 1995 earthquake and the coseismic and post-seismic period associated with the 2007 earthquake could represent a change in the geometry of the fault plane.

These characteristics suggested in the region of the Mejillones Peninsula are consistent with geometrical barrier models, such as the fragmentation barrier model described by King (1986). According to this model, the region around the barrier would be fractured by secondary structures (the process zone) and the normal faults could represent some of these secondary fractures. The fragmentation barrier model also establishes that a slip deficit remains in the barrier region after a main event has occurred in an adjacent segment, keeping the barrier area under high state of stress. This local concentration of stress may generate aftershocks, background seismicity and creep, as well as inelastic deformation in the process zones (e.g. Vermylie & Scholz 1998). The occurrence, under the region of the Mejillones Peninsula, of concentrated aftershock activity after the 1995 Antofagasta and 2007 Tocopilla earthquakes and of significant post-seismic deformation are thus consistent with the fragmentation barrier model. The initiation of the 1995 Antofagasta earthquake beneath the southern extremity of the Mejillones Peninsula could be explained as a consequence of local stress concentration there. This is also consistent with geometrical barrier models predicting that large earthquakes should nucleate in the vicinity of those barriers (e.g. Aki 1979; King 1986).

5.3 Relation between areas with different slip behaviour

According to friction laws, areas in a fault plane can be in three different frictional regimes: the unstable field (the only regime where earthquakes may nucleate), the conditionally stable field (where rupture can propagate) and the stable field (where rupture propagation will rapidly terminate) (see Scholz 1998 for a revision). In subduction zones, a seismogenic zone composed of a mixture of patches of material in contact in either the unstable, conditionally stable or stable fields of frictional sliding has been proposed (e.g. Lay & Kanamori 1981; Kanamori & McNally 1982; Scholz 1990; Pacheco *et al.* 1993; Bilek & Lay 2002; Igarashi *et al.* 2003). The maximum size of earthquakes in a region would be controlled by the size of the unstable regions or asperities. Therefore, the lower seismogenic zone where the 2007 Tocopilla earthquake ruptured could be characterized by smaller asperities than those in the upper seismogenic zone, that was ruptured by great earthquakes like the 1877 *M*w 8.8 event (that probably propagate downdip the lower zone). According to our preferred model, the size of larger asperities is $\sim 40 \times 40$ km, capable of generating $7 < M\text{w} < 7.5$ earthquakes (note that this is approximate, as the size of the patches strongly depends on the smoothing factor). Looking into details, patches of post-seismic slip in the models of Fig. 6 seem to concentrate within regions that exhibit low coseismic slip (Fig. 5a), suggesting that the afterslip distribution during the first month of the post-seismic interval complements the coseismic slip. Except for the patch labelled 1 in Fig. 6(a), the remaining post-seismic patches seem to have essentially slipped aseismically (deduced from the comparison of moment released by aftershocks in the same period). They could thus be interpreted as regions with aseismic behaviour (within the conditionally stable regime) in contact with the seismic patches that ruptured during the main shock. Nevertheless, it is worthy to notice that due to the small amplitude of these post-seismic slip patches (e.g. patches 4 and 5 in Fig. 6, $\sim$2 cm or less) the confidence in this complementarity is poor.

In the Antofagasta region, a heterogeneous slip behaviour of the lower seismogenic zone has been suggested due to successive seismic slips and creep pulses (Chlieh *et al.* 2004; Pritchard & Simons 2006; Pritchard *et al.* 2006, see Section 2 for more details). North of the Mejillones Peninsula, a partially coupled zone between 35–50 km depth was suggested by Chlieh *et al.* (2004) to model their interseismic geodetic measurements. Based on this interseismic model and the seismic and aseismic phenomena observed further South, before, during and after the Antofagasta earthquake, they proposed that aseismic shear and seismic slip could coexist there.

The lower seismogenic zone broken by the Tocopilla earthquake may also be characterized by an heterogeneous frictional structure and be the locus of both seismic rupture that would break locked asperities of moderate size and undergo pulses of aseismic slip between those asperities during the post- or interseismic periods. The upper seismogenic zone, where great earthquakes nucleate, is probably less heterogeneous and composed by larger asperities. Several studies have discussed the causal relationship between moderate-to-large earthquakes occurring in the lower seismogenic zone (1987 *M*w 7.5 and 1998 *M*w 7.1 earthquakes) and larger earthquakes that

mainly rupture its shallower part but also propagate downdip such as the 1995 *M*w 8.1 earthquake (Ihmlé & Ruegg, 1997; Pritchard *et al.* 2002; Chlieh *et al.* 2004). The 2007 Tocopilla earthquake is not an aftershock of a larger shallower earthquake but rather resembles the 1987 earthquake that preceded the 1995 Antofagasta earthquake. This suggests that the 2007 earthquake could trigger a larger earthquake updip. Although it has been proposed that the region updip Tocopilla rupture could be partially aseismic on the basis of Trench-Parallel Gravity Anomaly (TPGA) values together with the absence of large earthquake since 1877 (Loveless *et al.* 2009), interseismic geodetic measurements, although sparse and poorly constraining far from the coast, seem to be more compatible with a locked seismogenic zone between earthquakes (Bevis *et al.* 2001; Khazaradze & Klotz 2003; Chlieh *et al.* 2004).

5.4 Slip deficit after the Tocopilla earthquake

Fig. 8 represents the cumulative seismic potency deficit (Pc) since the last subduction mega-earthquake in North Chile (*M*w 8.8, 1877 May 10) and South Peru (*M*w 8.8, 1868 August 16) versus the released seismic potency (Pr) along strike during the *M*w > 7 earthquakes that occurred in this region. Seismic potency multiplied by the shear modulus equals the moment. The seismic potency released during the large 1995 Antofagasta and 2001 Arequipa earthquakes is shown as a reference for the northward and southward limits of the present day North Chile seismic gap (see text of Fig. 8 for details). The cumulative seismic potency has been calculated taking into account the convergence rate (6.4 cm yr^{-1}, Angermann *et al.* 1999) and the time elapsed since the last mega-earthquake (130 yr for simplicity in both 1877 and 1868 seismic gaps). The reasoning assumes, on one hand, that the 1877 and 1868 earthquakes released the whole interseismic slip deficit, so that the system was reset to zero and resumed interseismic stress accumulation from that moment, on a fully locked interface (i.e. no significant slip has been released aseismically by short- or long-term post-seismic deformation after the 1877 and 1868 earthquakes, slow slip events or similar aseismic processes).

Based on this end member model, ∼8.5 m of slip would have accumulated on the subduction interface before the occurrence of the Tocopilla earthquake along the 500 km fault length of the gap (red arrow in Fig. 8). Taking into account a fully coupled seismogenic zone of 117 km width (for a seismogenic depth of 50 km), we obtain a cumulative magnitude of *M*w 8.7 (∼*M*w 8.6 for a partially coupled zone as suggested by Chlieh *et al.* 2004). This corresponds to a cumulated seismic potency of 395 km^3. The Tocopilla earthquake generated an average slip of 1.2 m on the deeper part of the southernmost 150 km of the seismic gap, releasing only ∼10 km^3 seismic potency. Only ∼2.5 per cent of the seismic potency accumulated in the last 130 yr has been released during the 2007 earthquake, implying that the seismic gap remains significantly loaded. Therefore, the potential for a *M*w 8.7 earthquake in the North Chile seismic gap remains similar than before the 2007 Tocopilla earthquake, with the difference that this earthquake has increased stress on adjacent regions, further north and updip the 2007 rupture area.

Although some studies have revealed that great earthquakes have repeatedly ruptured this segment in the past (Comte & Pardo 1991; Vargas *et al.* 2005), they lack details in estimating the date and magnitude of those events. We can not discriminate whether this region pre-dominantly ruptured in similar great earthquakes of *M* ∼ 8.8, with regular recurrence intervals of ∼111 ± 33 yr (Comte & Pardo 1991) according to the characteristic earthquake model (Schwartz and Coppersmith 1984), or whether the interval between great earthquakes is larger because of the occurrence of smaller earthquakes (∼*M* 7–8), as it seems to be case in other subduction zones (e.g. Ecuador–Colombia subduction zone, Kanamori & McNally 1982; Sumatran subduction zone, Chlieh *et al.* 2007). In the first case, the next earthquake in the North Chile gap should be a great event rupturing the whole segment. In the latter case, series of shallow *M*w 8 earthquakes could rupture smaller segments of the current seismic gap in the years/centuries to come, while Tocopilla similar earthquakes, preceding or following the shallow events, could rupture the deep seismogenic zone. This second hypothesis is in better

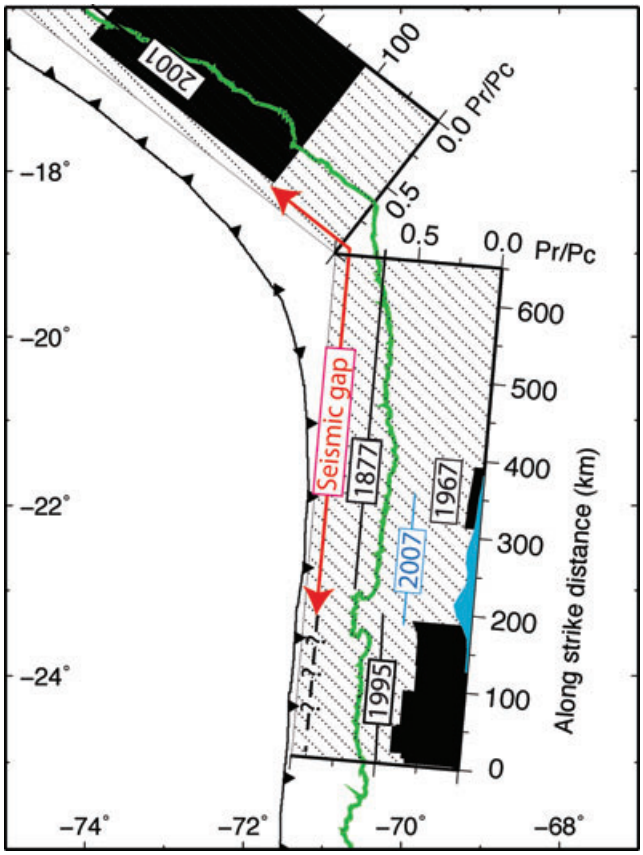

Figure 8. Seismic potency deficit along strike in the North Chile–South Peru subduction zone after the Tocopilla earthquake. Striped area represents interseismic potency cumulated (Pc) since 1877 in the North Chile gap and 1968 in the South Peru gap for a 100 per cent locking of the thrust interface between the Nazca and South American plates during the interseismic period and 6.4 cm yr^{-1} of convergence rate (Angermann *et al.*, 1999). Blue area represents the seismic potency released (Pr) during the 2007 Tocopilla main shock, its two *M*w ≥ 6 aftershocks on 2007 November 15 and the two post-seismic periods studied (cGPS-post1 and cGPS-post2). Black areas represent the seismic potency released during other *M*w ≥ 7 earthquakes occurred in the region (see Fig. 1). Note that several *M*w ≥ 7 in the region of Antofagasta (*M*w 7.5 1987, *M*w 7.0 1988, *M*w 7.2 1988 and *M*w 7.1 1998) are included in the Pr estimation, although they are not labelled. In the case of the 1995 Antofagasta, 2001 Arequipa and 2007 Tocopilla earthquakes, the seismic potency released during the post-seismic period is also included (20 per cent of the coseismic moment for the *M*w 8.1 Antofagasta earthquake, Chlieh *et al.* 2004; Pritchard & Simons 2006; 40 per cent of the coseismic moment for the *M*w 8.4 Arequipa earthquake, Ruegg *et al.* 2001; Melbourne *et al.* 2002; Pritchard 2003; 5 per cent of the coseismic moment for the 2007 Tocopilla earthquake, this work). Question marks indicate that the potency cumulated before the 1995 earthquake is uncertain in this region Coastline (green line) and trench (barbed line) have been superposed as reference.

agreement with the Gutenberg–Richter law (Gutenberg & Richter 1954), and great earthquakes capable of rupturing the complete seismic gap should occur occasionally, after several occurrences of smaller events.

6 CONCLUSIONS

Our analysis of InSAR and GPS measurements of the 2007 Tocopilla earthquake reveals that the main shock ruptured the deeper part of the seismogenic interface (between 30–50 km depth), with coseismic slip concentrated as two main asperities. The rupture did not propagate up to the trench, suggesting the seismogenic zone can be separated at 30 km depth into two regions with different behaviour. The 30-km depth limit could correspond to a change in geometry and/or a change in the frictional properties: the shallower seismogenic zone with potentially bigger asperities (since it has probably broken during the very large Mw 8.8 subduction earthquake in 1877) and a deeper region characterized by a more heterogeneous slip behaviour, capable of generating alone (without rupture of the shallower region) smaller earthquakes (of moderate magnitude: $7 \leq M < 8$). The downdip limit of the rupture seems to coincide with the downdip limit of the seismogenic zone (at ∼50 km depth), which seems to be controlled in this region by the intersection of the continental Moho with the subduction interface. Laterally, the 2007 rupture was arrested in its southern end beneath the Mejillones Peninsula, an intersegment zone characterized by structural complexity and occurrence of aseismic slip after large earthquakes rupturing one or another of the segments located north and south of it.

The post-seismic deformation appears associated to both, aftershocks and aseismic creep. Most of that post-seismic deformation has occurred during the first month after the main shock and it appears concentrated within regions that previously underwent low coseismic slip, especially the region close to the southern end of the rupture under the Mejillones Peninsula. The presence of both, seismic and aseismic slip patches under the Mejillones Peninsula region suggests a heterogeneous frictional behaviour of the subduction interface associated with the structural complexity of the overriding plate.

The Tocopilla earthquake ruptured partially the deeper part of the subduction interface over a length of 150 km in the southernmost part of the North Chile seismic gap (which has a total length of 500 km). It has released 2.5 per cent of the total moment deficit accumulated in the seismic gap since the 1877 Mw 8.8 earthquake. We note that the 2007 Mw 7.7 Tocopilla earthquake is similar to the Mw 7.5 earthquake that broke in 1987 the deeper region of the seismogenic interface, immediately downdip of the centroid of the 1995 Mw 8.1 Antofagasta earthquake, which ruptured south of the Mejillones Peninsula the shallower part of the subduction interface.

ACKNOWLEDGMENTS

We thank Matt Pritchard, an anonymous reviewer and Editor Duncan Agnew for thorough reviews that helped to improve the manuscript. This work was performed in the frame of the French/Chilean international collaboration (CNRS/CONICYT LIA 'Montessus de Ballore'). We thank the European Space Agency (ESA) for providing the ENVISAT images (project AO-720). This work was made possible thanks to the funding of the French National Research Agency (ANR-05-CATT-014, ANR-06-CATT-010-01), CNRS/INSU (funding of post-seismic task force), ARCUS project and BQR IPGP. The Caltech component of the GPS network was made possible by support from the Gordon and Betty Moore Foundation. MBP was partly supported by a grant of the Universidad Complutense de Madrid, CNRS and an Eiffel fellowship. DC was supported by an Ile-de-France Postdoctoral Fellowship and IPGP. GMT was used to create most of the figures (Wessel & Smith 1998). We thank C. Lasserre and R. Grandin for the linear inversion code. We thank S. Peyrat, P. Bernard, J.P. Vilotte, R. Madariaga, M. Sobiesiak, R. Lacassin, A. Coudurier Curveur and J.J. Martínez-Díaz for scientific discussion. This is IPGP contribution number 3032.

REFERENCES

Aki, K., 1979. Characterization of barriers on an earthquake fault, *J. geophys. Res.,* **84,** 6140–6148.

Allmendinger, R.W. & Gonzalez, G., 2009. Neogene to quaternary tectonics of the coastal Cordillera, northern Chile, *Tectonophysics,* in press, doi:10.1016/j.tecto.2009.04.019.

Altamimi, Z., Collilieux, X., Legrand, J., Garayt, B. & Boucher, C., 2007. ITRF2005: a new release of the International Terrestrial Reference Frame based on time series of station positions and Earth Orientation Parameters, *J. geophys. Res.,* **112,** B09401, doi:10.1029/2007JB004949.

ANCORP Working Group, 2003. Seismic imaging of a convergent continental margin and plateau in the central Andes (Andean Continental Research Project 1996 (ANCORP'96)), *J. geophys. Res.,* **108,** 2328, doi:10.1029/2002JB001771.

Angermann, D., Klotz, J. & C. Reigber, C., 1999. Space-geodetic estimation of the Nazca-South America Euler vector, *Earth planet. Sci. Lett,* **171,** 329–334.

Armijo, R. & Thiele, R., 1990. Active faulting in northern Chile: ramp stacking and lateral decoupling along a subduction plate boundary? *Earth planet. Sci. Lett,* **98,** 40–61.

Árnadóttir, T. & Segall, P., 1994. The 1989 Loma Prieta earthquake imaged from inversion of geodetic data, *J. geophys. Res.,* **99**(B11), doi:10.1029/94JB01256.

Baba, T., Hirata, K., Hori, T. & Sakaguchi, H., 2006. Offshore geodetic data conducive to the estimation of the afterslip distribution following the 2003 Tokachi-oki earthquake, *Earth planet. Sci. Lett.,* **241,** 281–292.

Beutler, G., Kouba, J. & Springer, T., 1993. Combining the orbits of the IGS processing centers, in *Proceedings of IGS Analysis Center Workshop,* pp. 20–56, ed. Kuba, J., Ottawa, Canada.

Bevis, M., Kendrick, E.C., Smalley R., Jr., Herring, T., Godoy, J. & Galban, F., 1999. Crustal motion north and south of the Arica deflection: comparing recent geodetic results from the central Andes, *Geochem. Geophys. Geosyst.,* **1**(12), 1005, doi:10.1029/1999GC000011.

Bevis, M., Kendrick, E., Smalley, R.J., Brooks, B.A., Allmendinger, R.W. & Isacks, B.L., 2001. On the strength of interplate coupling and the rate of back arc convergence in the central Andes: an analysis of the interseismic velocity field, *Geochem. Geophys. Geosyst.,* **2**(11), 1067, doi:10.1029/2001GC000198.

Bilek, S.L. & Lay, T., 2002. Tsunami earthquakes possibly widespread manifestations of frictional conditional stability, *Geophys. Res. Lett.,* **29**(14), 1673, doi:10.1029/2002GL015215.

Bürgmann, R., Kogan, M.G., Levin, V.E., Scholz, C.H., King, R.W. & Steblov, G.M., 2001. Rapid aseismic moment release following the 5 December 1997 Kronotsky Kamchatka earthquake, *Geophys. Res. Lett.,* **28,** 1331–1334.

Çakir, Z., de Chabalier, J.B., Armijo, R., Meyer, B., Barka, A. & Peltzer, G., 2003. Coseismic and early postseismic slip associated with the 1999 Izmit earthquake (Turkey), from SAR interferometry and tectonic field observations, *Geophys. J. Int.,* **155,** 93–110.

Cattin, R., Briole, P., Lyon-Caen, H., Bernard, P. & Pinettes, P., 1999. Effects of superficial layers on coseismic displacements for a dip-slip fault and geophysical implications, *Geophys. J. Int.,* **137,** 149–158.

Cavalié, O., Lasserre, C., Doin, M.P., Peltzer, G., Sun, J., Xu, X. & Shen, K., 2008. Measurement of interseismic strain across the

Haiyuan fault (Gansu, China), by InSAR, *Earth planet. Sci. Lett.,* doi:10.1016/j.epsl.2008.07.057.

Chlieh, M., de Chabalier, J.B., Ruegg, J.C., Armijo, R., Dmowska, R., Campos, J. & Feigl, K.L., 2004. Crustal deformation and fault slip during the seismic cycle in the North Chile subduction zone, from GPS and InSAR observations, *Geophys. J. Int.,* **158**(2), 695–711.

Chlieh, M. *et al*., 2007. Coseismic slip and afterslip of the great Mw 9.15 Sumatra–Andaman Earthquake of 2004, *Bull. seism. Soc. Am.,* **97,** 152–173, doi:10.1785/0120050631.

Cifuentes, I.L. & Silver, P.G., 1989. Low-frequency source characteristics of the great 1960 Chilean earthquake, *J. geophys. Res.,* **94**(B1), 643–663.

Comte, D. & Pardo, M., 1991. Reappraisal of great historical earthquakes in the northern Chile and southern Peru seismic gaps, *Nat. Hazards,* **4,** 23–44.

Comte, D. & Suárez, G., 1995. Stress distribution and geometry of the subducting Nazca plate in northern Chile using teleseismically recorded earthquakes, *Geophys. J. Int.,* **122,** 419–440.

Delouis, B., Cisternas, A., Dorbath, L., Rivera, L. & Kausel, E., 1996. The Andean subduction zone between 22° S and 24° S (northern Chile): precise geometry and state of stress, *Tectonophysics,* **259,** 81–100.

Delouis, B. *et al*., 1997. The MW = 8.0 Antofagasta (northern Chile) earthquake of 30 July 1995: a precursor to the end of the large 1877 gap, *Bull. seism. Soc. Am.,* **87,** 427–445.

Delouis, B., Pardo, M., Legrand, D. & Monfret, T., 2009. The Mw 7.7 Tocopilla earthquake of 14 November 2007 at the Southern Edge of the Northern Chile seismic gap: rupture in the deep part of the Coupled Plate Interface, *Bull. seism. Soc. Am.,* **99,** 87–94.

Dorbath, L., Cisternas, A. & Dorbath, C., 1990. Quantitative assessment of great earthquakes in Peru, *Bull. seism. Soc. Am.,* **80,** 551–576.

Du, Y., Aydin, A. & Segall P., 1992. Comparison of various inversion techniques as applied to the determination of a geophysical deformation model for the 1983 Borah Peak earthquake, *Bull. seism. Soc. Am.,* **82**(4), 1840–1866.

Engdahl, E.R. & Villaseñor, A., 2002. Global Seismicity: 1900–1999, in *International Handbook of Earthquake and Engineering Seismology,* pp. 665–690, eds Lee, W.H.K., Kanamori, H., Jennings, P.C. & Kisslinger, C., Part A, Chapter 41, Academic Press, San Diego, CA.

Farr, T.G. & Kobrick, M., 2000. Shuttle Radar Topography Mission produces a wealth of data, *EOS, Trans. Am. geophys. Un.,* **81**(48), 583–585.

Fitch, T.J., 1972. Plate convergence, transcurrent faults and internal deformation adjacent to the southeast Asia and western Pacific, *J. geophys. Res,* **77,** 4432–4460.

Grandin, R. *et al*., 2009. September 2005 Manda Hararo-Dabbahu rifting event, Afar (Ethiopia): constraints provided by geodetic data, *J. geophys. Res.,* **114,** B08404, doi:10.1029/2008JB005843.

Gutenberg, B. & Richter, C.F., 1954. Frequency and energy of earthquakes, in *Seismicity of the Earth and Associated Phenomena,* pp. 17–19, 2nd edn, Princeton University Press, Princeton, NJ.

Hanssen, R., 2001. *Radar Interferometry: Data Interpretation and Error Analysis,* Springer, New York.

Harris, R.A. & Segall, P., 1987. Detection of a locked zone at depth on the Parkfield, California, segment of the San Andreas fault, *J. geophys. Res.,* **92,** 7945–7962.

Hayes, G.P. & Wald, D.J., 2009. Developing framework to constrain the geometry of the seismic rupture plane on subduction interfaces a priori: a probabilistic approach, *Geophys. J. Int.,* **176,** 951–964, doi:10.1111/j.1365-246X.2008. 04035.x.

Hayes, G.P., Wald, D.J. & Keranen, K., 2009. Advancing techniques to constrain the geometry of the seismic rupture plane on subduction interfaces a priori: higher-order functional fits, *Geochem. Geophys. Geosyst.,* **10,** Q09006, doi:10.1029/2009GC002633.

Heki, K., Miyazaki, S. & Tsuji, H., 1997. Silent fault slip following an interplate thrust earthquake at the Japan Trench, *Nature,* **386,** 595–598.

Herring, T.A., Davis, J.L. & Shapiro, I.I., 1990. Geodesy by radio interferometry: the application of Kalman filtering to the analysis of very long baseline interferometry data, *J. geophys. Res.,* **95**(B8), 12 561–12 581.

Hsu, Y.J. *et al*., 2006. Frictional afterslip following the 2005 Nias-Simeulue earthquake, Sumatra, *Science,* **312,** 1921–1926.

Hyndman, R.D. & Wang, K., 1993. Thermal constraints on the zone of major thrust earthquake failure: the Cascadia subduction zone, *J. geophys. Res.,* **98,** 2039–2060.

Igarashi, T., Matsuzawa, T. & Hasegawa, A., 2003. Repeating earthquakes and interplate aseismic slip in the northeastern Japan subduction zone, *J. geophys. Res.,* **108**(B5), 2249, doi:10.1029/2002JB001920.

Ihmlé, P.F. & Ruegg, J.C., 1997. Source tomography by simulatedannealing using broad-band surface waves and geodetic data: application to the Mw = 8.1 Chile 1995 event, *Geophys. J. Int.,* **131,** 146–158.

Jonsson, S., Zebker, H., Segall, P. & Amelung, F., 2002. Fault slip distribution of the 1999 Mw 7.1 Hector Mine, California, earthquake, estimated from satellite radar and GPS measurements, *Bull. seism. Soc. Am.,* **92**(4), 1377–1389.

Kanamori, H. & McNally, K., 1982. Variable rupture mode of the subduction zone along the Ecuador-Colombia coast, *Bull. seism. Soc. Am.,* **72,** 1241–1253.

Kelleher, J.A., 1972. Rupture zones of large south America earthquakes and some predictions, *J. geophys. Res.,* **77,** 2087–2103.

Khazaradze, G., & Klotz, J., 2003. Short and long-term effects of GPS measured crustal deformation rates along the South-Central Andes, *J. geophys. Res.,* **108**(B4), 1–13.

King, G.C.P., 1986. Speculations on the geometry of the initiation and termination processes of earthquake rupture and its relation to morphology and geological structure, *Pure appl. Geophys.,* **124**(3), 567–585.

King, R.W. & Bock, Y., 2000. *Documentation for the GAMIT GPS Software Analysis Version 9.9, 365 Mass,* Inst. of Technol., Cambridge.

Klotz, J. *et al*., 1999. GPS-derived deformation of the central Andes including the 1995 Antofagasta Mw = 8.0 earthquake, *Pure appl. Geophys.,* **154,** 3709–3730.

Lasserre C., Peltzer G., Crampé F., Klinger Y., Van Der Woerd J., Tapponnier P., 2005. Coseismic deformation of the 2001 Mw = 7.8 Kokoxili earthquake in Tibet, measured by SAR interferometry, *J. geophys. Res.,* **110**(B12), B12408, doi:10.1029/2004JB003500.

Lay, T. & Kanamori, H., 1981. An asperity model of large earthquake sequences, in *Earthquake Prediction: An International Review, Maurice Ewing Series **4***, pp. 579–592, eds Simpson, D.W. & Richards, P.G., AGU, Washington, DC.

Lohman, R.B. & Simons, M., 2005. Some thoughts on the use of InSAR data to constrain models of surface deformation: noise structure and data downsampling, *Geochem. Geophys. Geosyst.,* **6,** Q01007, doi:10.1029/2004GC000841.

Loveless, J.P., Pritchard, M.E. & Kukowski, N., 2009. Testing mechanisms of subduction zone segmentation and seismogenesis with slip distributions from recent Andean earthquakes, *Tectonophysics,* doi:10.1016/j.tecto.2009.05.008, in press.

Malgrange, M. & Madariaga, R., 1983. Complex distribution of large thrust and normal fault earthquakes in the Chilean subduction zone, *Geophys. J. R. astr. Soc.,* **73,** 489–505.

Marone, C.J., Scholz, C.H. & Bilham, R., 1991. On the mechanics of earthquake afterslip, *J. geophys. Res.,* **96,** 8441–8452.

Massonnet, D. & Feigl, K., 1998. Radar interferometry and its application to changes in the earth's surface, *Rev. Geophys.,* **36,** 441–500.

Melbourne, T., Webb, F., Stock, J. & Reigber, C., 2002. Rapid post-seismic transients in subduction zones from continuous GPS, *J. geophys. Res.,* **107**(B10), 2241, doi:10.1029/2001JB000555.

Menke, W., 1989. *Geophysical Data Analysis: Discrete Inverse Theory,* Rev. ed., Academic, New York.

Miyazaki, S., Segall, P., Fukuda, J. & Kato, T., 2004. Space time distributions of afterslip following the 2003 Tokachi-oki earthquake: implications for variations in fault zone frictional properties, *Geophys. Res. Lett.,* **31,** doi:10.1029/2003GL019410.

Mogi, K., 1985. Temporal variation of crustal deformation during the days preceding a thrust-type great earthquake: the 1944 Tonankai earthquake of magnitude 8.1, Japan, *Pure appl. Geophys.,* **122,** 765–780.

Monfret, T., Dorbath, L., Caminade, J.P., Pardo, M., Comte, D. & Ponce, L., 1995. The July 30, Antofagasta earthquake: an ''Hypocritical'' seismic event, *EOS, Trans. Am. geophys. Un.,* **76,** 427.

Nishenko, S.P., 1985. Seismic potential for large and great interplate earthquakes along the Chilean and southern Peruvian margins of South America: a quantitative reappraisal, *J. geophys. Res.,* **90,** 3589–3615.

Norabuena, E.O., Dixon, T.H., Stein, S. & Harrison, C.G.A., 1999. Decelerating Nazca-South America and Nazca-Pacific plate motion, *Geophys. Res. Lett.,* **26**(22), 3405–3408.

Okada, Y., 1985. Surface deformation to shear and tensile faults in a half space, *Bull. seism. Soc. Am.,* **75,** 1135–1154.

Oleskevich, D.A., Hyndman, R.D. & Wang, K., 1999. The updip and downdip limits to great subduction earthquakes: thermal and structural models of Cascadia, south Alaska, SW Japan, and Chile, *J. geophys. Res.,* **104,** 14 965–14 991, doi:10.1029/1999JB900060.

Pacheco, J., Sykes, L. & Scholz, C., 1993. Nature of seismic coupling along simple plate boundaries of the subduction type, *J. geophys. Res.,* **98,** 14133–14159.

Patzwahl, R., Mechie, J., Schulze, A. & Giese, P., 1999. Two-dimensional velocity models of the Nazca plate subduction zone between 19.5_S and 25_S from wide-angle seismic measurements during the CINCA95 project, *J. geophys. Res.,* **104,** 7293–7317.

Perfettini, H. & Avouac, J.P., 2004. Postseismic relaxation driven by brittle creep: a possible mechanism to reconcile geodetic measurements and the decay rate of aftershocks, application to the Chi-Chi earthquake, Taiwan, *J. geophys. Res.,* **109,** B02304, doi:10.1029/2003JB002488.

Peyrat, S., Madariaga, R., Buforn, E., Campos, J., Asch, G. & Vilotte, J.P., 2010. Kinematic rupture process of the 2007 Tocopilla earthquake and its main aftershocks from teleseismic and strong motion data, *Geophys. J. Int.*, **182,** 1411–1430.

Pritchard, M.E., 2003. Recent crustal deformation in west-central South America, *PhD thesis*. Calif. Inst. of Technol., Pasadena.

Pritchard, M.E., Simons, M., Rosen, P., Hensley, S. & Webb, F., 2002. Coseismic slip from the 1995 July 30 MW = 8.1 Antofagasta, Chile, earthquake as constrained by InSAR and GPS observations, *Geophys. J. Int.,* **150,** 362–376.

Pritchard, M.E., Ji, C. & Simons, M., 2006. Distribution of slip from 11 Mw > 6 earthquakes in the northern Chile subduction zone, *J. geophys. Res.,* **111,** doi:10.1029/2005JB004013.

Pritchard, M.E. & Simons, M., 2006. An aseismic fault slip pulse in northern Chile and along-strike variations in seismogenic behavior, *J. geophys. Res.,* **111,** B08405, doi:10.1029/2006JB004258.

Pritchard, M.E., Norabuena, E.O., Ji, C., Boroschek, R., Comte, D., Simons, M., Dixon, T. & Rosen, P.A., 2007. Geodetic, teleseismic and strong motion constraints on slip from recent southern Peru subduction zone earthquakes, *J. geophys. Res.,* **112,** B03307, doi:10.1029/2006JB004294.

Puysségur, B., Michel, R. & Avouac, J.P., 2007. Tropospheric phase delay in interferometric synthetic aperture radar estimated from meteorological model and multispectral imagery, *J. geophys. Res.,* **112,** B05419, doi:10.1029/2006JB004352.

Rosen, P., Hensley, S., Peltzer, G. & Simons, M., 2004. Updated repeat orbit interferometry package released, *EOS, Trans. Am. geophys. Un.,* **85,** 47.

Rosenbaum G., Giles D., Saxon M., Betts P.G., Weinberg R.F. & Duboz C., 2005. Subduction of the Nazca Ridge and the Inca Plateau: insights into the formation of ore deposits in Peru, *Earth planet. Sci. Lett.,* **239,** 18–32, doi:10.1016/j.epsl.2005.08.003.

Ruegg, J.C. *et al*., 1996. The Mw = 8.1 Antofagasta (North Chile) earthquake of July 30, 1995: first results from teleseismic and geodetic data, *Geophys. Res. Lett.,* **23,** 917–920.

Ruegg, J.C., Olcay, M. & Lazo, D., 2001. Co-, post- and pre (?)-seismic displacements associated with the Mw = 8.4 southern Peru earthquake of 23 June 2001 from continuous GPS measurements, *Seismol. Res. Lett.,* **72,** 673–678.

Scholz, C., 1990. *The Mechanics of Earthquakes and Faulting,* p. 439, Cambridge University Press, New York.

Scholz, C.H., 1998. Earthquakes and friction laws, *Nature,* **391,** 37–42.

Schwartz, D.D. & Coppersmith, K.J., 1984. Fault behavior and characteristic earthquakes: examples from the Wasatch and San Andreas Fault Zones, *J. geophys. Res.,* **89,** 5681–5698.

Schwartz, S.Y. & Rokosky, J.M., 2007. Slow slip events and seismic tremor at circum-pacific subduction zones, *Rev. Geophys.,* **45,** RG3004, doi:10.1029/2006RG000208.

Sella, G.F., Dixon, T.H. & Mao, A., 2002. REVEL: a model for recent plate velocities from space geodesy, *J. geophys. Res.,* **107**(B4), doi:10.1029/2000JB000033.

Song, T.R.A. & Simons, M., 2003. Large trench-parallel gravity variations predict seismogenic behavior in subduction zones, *Science,* **301,** 630–633.

Suarez, G. & Comte, D., 1993. Comment on "Seismic Coupling Along the Chilean Subduction Zone", by B. W. Tichelaar and L. R. Ruff, *J. geophys. Res.,* **98**(B9), 15 825–15 828.

Tarantola, A. & Valette, B., 1982. Generalized nonlinear inverse problem solved using the least squares criterion, *Rev. Geophys.,* **20,** 219–232.

Tichelaar, B.W. & Ruff, L.J., 1991. Seismic coupling along the Chilean subduction zone, *J. geophys. Res.,* **96,** 11 997–12 022.

Vargas, G., Ortlieb, L., Chapron, E., Valdés, J. & Marquardt, C., 2005. Paleoseismic inferences from a high resolution marine sedimentary record in northern Chile (23°S), *Tectonophysics,* **399,** 381–398.

Vigny, C., Rudloff, A., Ruegg, J.C., Madariaga, R., Campos, J. & Alvarez, M., 2009. Upper plate deformation measured by GPS in the Coquimbo gap, Chile, *Phys. Earth planet. Inter.,* **175**(1–2), 86–95.

Wessel, P. & Smith, W.H.F., 1998. New, improved version of Generic Mapping Tools released, *EOS, Trans. Am. geophys. Un.,* **79,** 579.

SUPPORTING INFORMATION

Additional Supporting Information may be found in the online version of this article:

Appendix A. Error associated to the InSAR data.
Appendix B. GPS data and time-series.
Appendix C. Comparison between data sets.
Appendix D. InSAR data subsampling.
Appendix E. Uniform slip model: comparison between several proposed geometries, uncertainties and residuals.
Appendix F. Smoothing.
Appendix G. Checkerboard resolution test.
Appendix H. Residuals.
Appendix I. Slip models (text files).

Please note: Wiley-Blackwell are not responsible for the content or functionality of any supporting materials supplied by the authors. Any queries (other than missing material) should be directed to the corresponding author for the article.